*minerals*

MDPI

*Article*

# Distribution and Mineralogical Characterization of Rare Earth and Uranium Minerals in Copper Flotation Tailings from Prominent Hill, South Australia

**Zina Habibi [1,*], Nigel J. Cook [1], Kathy Ehrig [1,2] and Cristiana L. Ciobanu [1]**

[1] School of Chemical Engineering, Adelaide University, Adelaide, SA 5005, Australia; nigel.cook@adelaide.edu.au (N.J.C.); kathy.ehrig@bhp.com (K.E.); cristiana.ciobanu@adelaide.edu.au (C.L.C.)
[2] BHP Copper South Australia, 10 Franklin Street, Adelaide, SA 5000, Australia
* Correspondence: zina.habibi@adelaide.edu.au

## Abstract

Fresh flotation tailings represent an underutilized archive of mineralogical and geochemical information in which multiple strands of evidence for ore-forming processes and post-depositional modification can be preserved. Detailed characterization of tailings is also vital for assessment of their future potential as a secondary source of recoverable by-products. This study investigates residual mineral speciation and mineral distributions in size fractions of tailings from the Prominent Hill iron oxide–copper–gold (IOCG) deposit, South Australia, with emphasis on rare earth element (REE) minerals and associated phases containing uranium (U). Assemblages of REE minerals can be highly complex at the micron scale and include sequences of mineral replacement, notably monazite → florencite, and monazite → synchysite. Bastnäsite-(Ce) commonly appears paragenetically early and is frequently altered or replaced by synchysite and parisite, supporting episodes of REE remobilization and reconcentration over geological time. Uranium is closely associated with REEs, and U-mineral assemblages are similarly characterized by intricate replacement relationships between uraninite and secondary phases. Uraninite is variably replaced by coffinite and the U-carbonate wyartite, reflecting changes in redox state, silica activity, and fluid composition. Additional replacement pathways from uraninite to Cu–Fe sulphides, including bornite and chalcopyrite, are documented and indicate coupled dissolution–reprecipitation of sulphides and U-minerals during superimposed hydrothermal activity. Preservation of mineralogical relationships within tailings drawn from multiple parts of a large deposit highlights their value as an essentially untapped library of information to reconstruct deposit evolution, complementing traditional study of selected drill core samples. Systematic investigation of tailings from large deposits can improve genetic models for large copper deposits, including but not restricted to IOCGs, and provide essential insights into REE behaviour, uranium remobilization, and critical metal potential. These findings emphasize the scientific and economic value of tailings-based studies for improved resource characterization, refining metallogenic interpretations, guiding future exploration strategies, and assessing opportunities for reprocessing and metal recovery in large ore systems worldwide across diverse geological settings.

**Keywords:** flotation tailings; iron oxide–copper–gold deposits; Prominent Hill; REE minerals; uraninite; coffinite; mineral replacement; uranium carbonates

Check for updates

Academic Editors: Jaroslav Dostal, David Lentz, Jia-Xi Zhou and Giovanni Grieco

Received: 14 May 2026
Revised: 22 June 2026
Accepted: 22 June 2026
Published: 25 June 2026

**Copyright:** © 2026 by the authors. Licensee MDPI, Basel, Switzerland. This article is an open access article distributed under the terms and conditions of the Creative Commons Attribution (CC BY) license.

## 1. Introduction

Iron oxide–copper–gold (IOCG) deposits are one of the most economically significant types of mineral systems, not only supplying copper and precious metals, but also exhibiting considerable potential as a viable source for a range of other strategically important by-product elements (e.g., [1–3]). Paramount among these are rare earth elements (REEs), which are commonly hosted as fluorocarbonates, phosphates, and various accessory mineral phases, as well as substituents in common ore and gangue minerals (e.g., [4,5]). Large-scale IOCG mining operations generate substantial volumes of tailings that retain complex mineralogical assemblages, including unrecovered REE-bearing phases, prompting efforts to identify economically viable options for their recovery as by-products (e.g., [6–9]). Such studies are, however, reliant on detailed and comprehensive understanding of the mineralogy and mineral composition of tailings, both fresh and in long-term tailings storage facilities. Likewise, understanding the geochemical behaviour of all contained elements, whether target or non-target, is critical if the resource potential is to be unlocked [10,11] and the environmental impact effectively managed.

The growing interest in REEs reflects their expanding role in modern society. Rare earths are indispensable to advanced technologies, including electronics, renewable energy systems, high-performance magnets, and defence applications [12]. The ability to access additional sources beyond primary REE-dominant orebodies has become increasingly important [9]. Stored flotation tailings, produced over decades of mining activity, represent a significant and readily accessible repository of these critical elements, with the potential to supplement traditional supply chains [13].

Uranium remains a cornerstone of nuclear energy production and is a common component of some IOCG-type ores, even if seldom present at concentrations allowing economic recovery [14]. At subeconomic concentrations, uranium is largely a nuisance component of these ores that can compromise concentrate quality and place additional demands on tailings management.

Detailed characterization of IOCG tailings from Carrapateena, South Australia, provides fundamental insights into the distribution, mode of occurrence, and mineral hosts for REEs [15]. REEs and associated HFSE elements are often finely disseminated or locked within refractory mineral phases that are not targeted during conventional processing to recover copper and contained precious metals. Advanced microanalytical techniques, including mineralogical, microstructural, and geochemical approaches, are essential to accurately identify patterns of REE deportment, determine the textural relationships of key minerals, and assess their association with iron oxides and other gangue phases. Augmented by the study of coexisting non-target minerals, including those containing U, such knowledge underpins the evaluation of tailings as secondary resources [15] and supports the development of targeted extraction and processing strategies [16].

The development of methodologies to characterize and potentially reprocess REE- and U-bearing tailings aligns with broader trends in improving resource efficiency while potentially benefitting from technological innovation within the mining sector [13,17]. By quantifying the mineralogical controls on element distribution and recovery, tailings characterization supports informed decision-making regarding processing optimization, resource valuation, and long-term planning of mining–processing operations. Moreover, it enables the mining industry to respond to evolving societal needs for secure and diversified supplies of critical raw materials, reinforcing the strategic importance of IOCG systems beyond production of copper and other primary metals.

There is currently a growing research focus on mine tailings in general to improve metallurgical performance and guide environmental and geotechnical management practices (e.g., [18,19]). Tailings are also recognized as repositories of unrecovered REEs and other critical elements [20]. Despite this, comprehensive characterization studies of IOCG tailings remain relatively limited, and few have examined the critical importance of size distribution and mineral association. Moreover, given the coexistence of REEs, uranium, and radionuclides resulting from decay of U and thorium (Th) within ore feed and in processing circuits for such ores [21–23], a sound understanding of the intimate textural relationships between REEs and phases containing U and its daughters is vital fundamental knowledge to support any recovery strategy. Important knowledge gaps include the texture- and size-dependency relationships among REE- and U-bearing mineral phases.

The characterization of fresh tailings from mining–processing operations such as Prominent Hill (South Australia), in which REE enrichment is recognized, has an important role to play in resolving such issues, in turn helping to determine factors that impact the viability of future REE recovery. Although finely ground tailings implicitly lack some geological information, examination of tens of thousands of tailings particles derived from a diverse range of ore facies located across a complex and lithologically diverse ore deposit carries the major advantage of being more representative than the more traditional characterization of samples selected (commonly with unintended bias) from drill cores.

By combining detailed mineralogical, microstructural, and geochemical analyses, this study aims to elucidate the principal hosts for REEs and associated U in tailings, replacement relationships among minerals, and the distribution patterns of individual mineral phases. This investigation not only enhances understanding of the controls on critical element capture and release within IOCG tailings but also provides a framework for evaluating tailings as potential sources of strategic elements in support of resource diversification and sustainable mineral utilization. In addition, emphasis is placed on the invaluable mineralogical information that careful characterization of tailings and their component minerals can deliver to complement existing models of ore genesis and subsequent evolution over geological time.

## 2. Prominent Hill Deposit

The Prominent Hill deposit is located within the Olympic Cu-Au Province of South Australia, a Mesoproterozoic metallogenic province situated on the eastern margin of the Gawler Craton (Figure 1). The province [24] hosts some of the world's largest (IOCG) systems, thus making it one of the world's most significant provinces for copper, gold, silver and uranium mineralization [25]. Major IOCG deposits, represented by the active mines and processing facilities at Olympic Dam, Carrapateena, and Prominent Hill, along with the recently discovered Oak Dam prospect, are broadly associated with ca. 1.60–1.57 Ga Gawler Range Volcanics and coeval Hiltaba Suite intrusions [26]. Mineralization is, in part, structurally controlled by long-lived crustal-scale fault systems that facilitated fluid flow, brecciation, and iron metasomatism, notably at Olympic Dam [27]. The resource endowment of the Olympic Cu-Au Province is dominated by the Olympic Dam deposit, which is by far the largest IOCG system. Olympic Dam is characterized by a broad alteration footprint and a marked enrichment in U compared to the other deposits, as well as REEs [27,28].

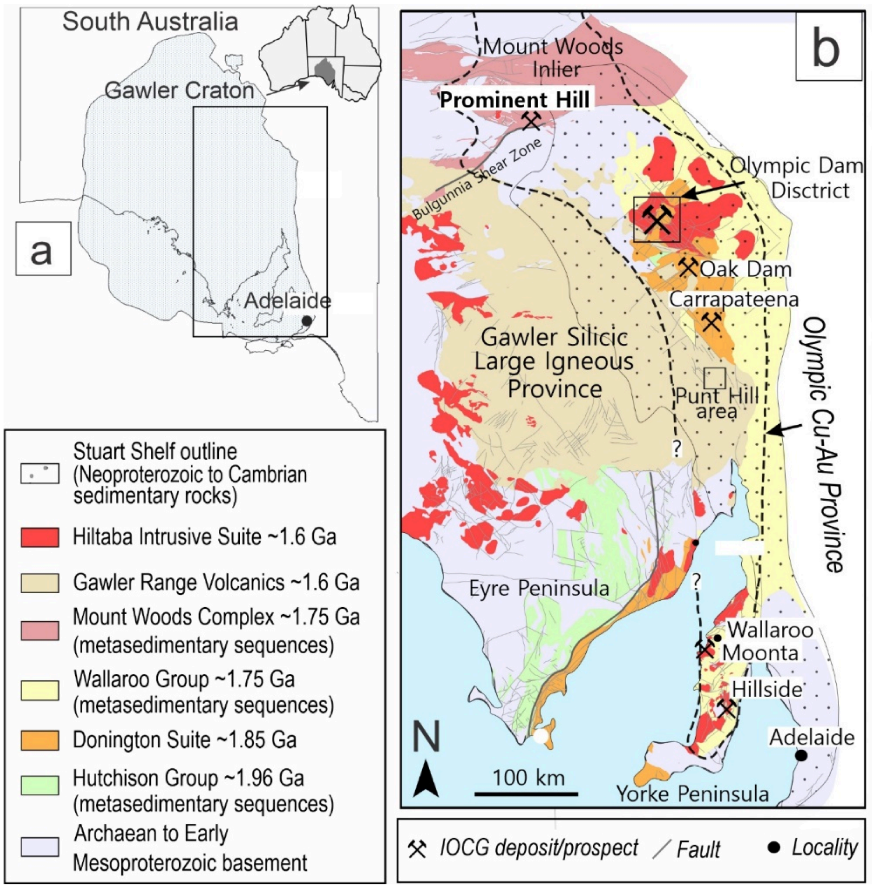



**Figure 1.** (**a**) Outline and location of Gawler Craton in South Australia. (**b**) Simplified geological map of eastern Gawler Craton (area marked as rectangle in (**a**)), showing the location of Prominent Hill alongside other major IOCG deposits in the Olympic Cu-Au Province (after [29]). Main lithologies and structures compiled from the Geological Survey of South Australia (https://map.sarig.sa.gov.au/).

The smaller Prominent Hill Cu-Au-Ag deposit is located on the southern margin of the Mount Woods Domain, ca. 150 km NW of Olympic Dam and 650 km NW of Adelaide. Like Olympic Dam, the deposit comprises hematite-dominated breccias developed within variably altered (meta)volcanic and metasedimentary rocks (e.g., [30,31]). The breccia complex also contains fragments of granitoid and porphyry that are considered part of the Gawler Range Volcanics/Hiltaba Suite magmatic event at 1600–1570 Ma [32]. U-Pb hematite ages (authors' unpublished data) yield ages of ~1595 Ma, firmly placing formation of the Prominent Hill deposit during the Gawler Range Volcanics/Hiltaba Suite magmatic event within the Olympic Cu–Au province. $^{40}$Ar–$^{39}$Ar dating of sericite from breccias in the southern part of the deposit yields a ~1575 Ma minimum age for sericitization [32], further corroborating formation of the Prominent Hill deposit during the Gawler Range Volcanics/Hiltaba Suite magmatic event.

Copper–gold mineralization is closely associated with intense iron oxide alteration and structurally controlled breccia systems [31,33,34]. The deposit was first discovered in 2001 [35], and the Prominent Hill mine was commissioned in 2009. Proven reserves at Prominent Hill as per 30 June 2025 comprise 26 Mt @ 1.07% Cu, 0.59 g/t Au, and 3 g/t Ag, with reported metallurgical recoveries of 88% for Cu and 72% for both Au and Ag. Prominent Hill produces one of the highest grades of copper concentrate in the world [36]. The present study addresses fresh tailings only. Information on tailings storage facilities at Prominent Hill is provided by Cooke [37].

## 3. Sampling and Methodology

### *3.1. Analytical Methodology*

This study addresses the variation in chemical composition, mineral abundance, and textures among minerals with respect to particle size. We have undertaken a µm-scale analysis of ten size fractions of a sample of fresh flotation tailings (PHRT) from the Prominent Hill processing plant (October 2023): +125 µm, +106 µm, +75 µm, +53 µm, +C1, +C3, +C4, +C5, +C6 and +C7. Particles from each fraction are mounted in a 2.5 cm diameter epoxy block and polished, exposing tens of thousands of individual particles at the surface. Mass balances are included in Table 1.

**Table 1.** Assay data for major elements and selected minor elements/traces, including lanthanides, in the head sample and each of the ten size fractions (in ppm, unless otherwise indicated). Size (in µm) and mass% proportions for each fraction are also indicated.

| Texture | Fraction | Size µm | Mass % | F * % | Al % | Ca % | Fe % | K % | Mg % | Mn % | Na % | P % | Si % | Ti % | $CO_2$ % |
|---|---|---|---|---|---|---|---|---|---|---|---|---|---|---|---|
| | PHRT Head | | | 0.39 | 3.92 | 1.60 | 26.07 | 2.03 | 0.98 | 0.09 | 0.11 | 0.18 | 19.76 | 0.30 | 2.76 |
| Coarse | PHRT + 125 | +125 | 12.3 | 0.36 | 4.60 | 1.72 | 11.14 | 2.40 | 1.16 | 0.09 | 0.05 | 0.13 | 28.93 | 0.33 | 3.27 |
| | PHRT + 106 | +106 | 4.7 | 0.34 | 3.91 | 1.63 | 16.93 | 2.04 | 1.03 | 0.09 | 0.05 | 0.15 | 25.54 | 0.32 | 3.14 |
| | PHRT + 75 | +75 | 10.9 | 0.34 | 3.34 | 1.43 | 23.58 | 1.74 | 0.88 | 0.08 | 0.04 | 0.15 | 22.41 | 0.30 | 2.72 |
| | PHRT + 53 | +53 | 13.0 | 0.30 | 2.76 | 1.26 | 31.19 | 1.42 | 0.73 | 0.07 | 0.04 | 0.14 | 18.63 | 0.28 | 2.34 |
| Fine | PHRT + C1 | +31 | 8.1 | 0.21 | 1.48 | 0.76 | 47.73 | 0.75 | 0.40 | 0.05 | 0.02 | 0.13 | 8.92 | 0.26 | 1.45 |
| | PHRT + C3 | +15 | 13.8 | 0.35 | 2.55 | 1.60 | 30.73 | 1.30 | 0.83 | 0.09 | 0.03 | 0.15 | 17.92 | 0.29 | 2.95 |
| | PHRT + C4 | +11 | 6.4 | 0.38 | 2.38 | 1.95 | 30.19 | 1.19 | 0.95 | 0.10 | 0.03 | 0.19 | 17.40 | 0.30 | 3.64 |
| | PHRT + C5 | +9 | 4.2 | 0.43 | 2.45 | 2.16 | 30.74 | 1.22 | 1.04 | 0.12 | 0.03 | 0.22 | 17.18 | 0.31 | 4.10 |
| | PHRT + C6 | +4 | 6.2 | 0.47 | 3.02 | 2.20 | 28.93 | 1.53 | 1.11 | 0.13 | 0.04 | 0.25 | 17.32 | 0.32 | 4.24 |
| Very fine | PHRT + C7 | −4 | 20.4 | 0.60 | 8.00 | 1.52 | 19.21 | 3.86 | 1.36 | 0.10 | 0.06 | 0.23 | 19.14 | 0.27 | 3.02 |
| **Texture** | **Fraction** | **Au *** | **Ag** | **As** | **Bi** | **Co** | **Cu** | **Mo** | **Ni** | **Pb** | **Sn** | **Th** | **$U_3O_8$** | **W** | **Zn** |
| | PHRT Head | 0.18 | 0.60 | 43.6 | 1.26 | 25.7 | 742 | 39 | 23 | 19 | 16 | 16.64 | 105 | 30 | 17 |
| Coarse | PHRT +125 | 0.30 | 0.97 | 31.4 | 1.50 | 28.8 | 1657 | 23 | 24 | 16 | 8 | 14.41 | 72 | 11 | 21 |
| | PHRT + 106 | 0.32 | 0.83 | 34.2 | 1.78 | 25.4 | 1298 | 31 | 21 | 17 | 11 | 15.66 | 77 | 17 | 17 |
| | PHRT + 75 | 0.26 | 0.60 | 40.9 | 1.37 | 22.1 | 993 | 40 | 19 | 18 | 15 | 15.11 | 82 | 26 | 16 |
| | PHRT + 53 | 0.24 | 0.83 | 49.0 | 1.22 | 20.2 | 734 | 45 | 17 | 20 | 21 | 13.73 | 91 | 37 | 15 |
| Fine | PHRT + C1 | 0.32 | 0.35 | 62.4 | 1.16 | 15.3 | 712 | 59 | 13 | 31 | 32 | 12.21 | 121 | 59 | 33 |
| | PHRT + C3 | 0.24 | 0.34 | 43.7 | 1.00 | 20.1 | 720 | 38 | 18 | 30 | 19 | 13.56 | 98 | 34 | 37 |
| | PHRT + C4 | 0.16 | 0.50 | 42.4 | 1.00 | 21.4 | 741 | 39 | 20 | 32 | 18 | 14.55 | 102 | 33 | 32 |
| | PHRT + C5 | I.S. | 0.31 | 42.4 | 0.96 | 23.7 | 678 | 39 | 22 | 51 | 17 | 16.16 | 107 | 31 | 39 |
| | PHRT + C6 | 0.11 | 0.36 | 42.8 | 1.06 | 26.9 | 650 | 39 | 26 | 47 | 17 | 19.11 | 111 | 29 | 58 |
| Very fine | PHRT + C7 | 0.11 | 0.98 | 46.5 | 1.66 | 43.3 | 947 | 36 | 44 | 34 | 12 | 21.66 | 136 | 16 | 61 |
| **Texture** | **Fraction** | **Y** | **La** | **Ce** | **Pr** | **Nd** | **Sm** | **Eu** | **Gd** | **Tb** | **Dy** | **Ho** | **Er** | **Tm** | **Yb** |
| | PHRT Head | 33.5 | 1001 | 1467 | 123 | 306 | 27.1 | 10.81 | 13.4 | 1.46 | 7.88 | 1.42 | 3.69 | 0.54 | 3.29 |
| Coarse | PHRT + 125 | 31.4 | 554 | 813 | 69.4 | 178 | 16.7 | 6.48 | 8.9 | 1.09 | 6.04 | 1.15 | 3.27 | 0.51 | 3.20 |
| | PHRT + 106 | 31.4 | 754 | 1116 | 93.0 | 229 | 21.9 | 8.32 | 10.2 | 1.43 | 6.43 | 1.27 | 3.50 | 0.50 | 3.39 |
| | PHRT + 75 | 28.6 | 794 | 1160 | 97.7 | 244 | 23.8 | 8.56 | 10.4 | 1.22 | 6.06 | 1.13 | 3.23 | 0.44 | 3.02 |
| | PHRT + 53 | 27.3 | 793 | 1161 | 96.9 | 242 | 22.7 | 8.27 | 10.0 | 1.22 | 5.67 | 1.09 | 2.84 | 0.40 | 2.58 |
| Fine | PHRT + C1 | 24.5 | 786 | 1152 | 96.9 | 246 | 23.0 | 8.29 | 9.51 | 1.09 | 5.44 | 0.96 | 2.51 | 0.38 | 2.34 |
| | PHRT + C3 | 30.6 | 791 | 1178 | 99.4 | 252 | 24.9 | 8.67 | 12.0 | 1.35 | 6.43 | 1.18 | 3.30 | 0.46 | 2.80 |
| | PHRT + C4 | 34.9 | 955 | 1456 | 127 | 321 | 30.8 | 11.20 | 14.4 | 1.59 | 7.78 | 1.47 | 3.62 | 0.53 | 2.99 |
| | PHRT + C5 | 39.8 | 1177 | 1800 | 157 | 405 | 39.2 | 14.30 | 18.0 | 2.00 | 8.94 | 1.63 | 4.00 | 0.63 | 3.30 |
| | PHRT + C6 | 45.3 | 1506 | 2322 | 201 | 510 | 50.1 | 17.80 | 22.0 | 2.42 | 10.8 | 1.83 | 4.76 | 0.61 | 3.59 |
| Very fine | PHRT + C7 | 47.4 | 1661 | 2343 | 199 | 478 | 39.9 | 16.10 | 18.7 | 2.23 | 11.3 | 1.96 | 5.50 | 0.82 | 4.57 |

Other minor elements assayed include Cr (61–223 ppm in all fractions), Sc (12 ppm in PHRT + C7, 4–8 ppm in all others), Nb (11.5–20.4 ppm in all fractions), Sb (<6 ppm in all fractions), Se (<3 ppm in all), Ta (<1 ppm), Te (2 ppm in PHRT + C7, <2 ppm in all others), Sr (367 ppm in PHRT + C7, 133–278 in all fractions), V (72–111 ppm in all), Zr (125–168 ppm in all fractions), and Lu (<1 ppm in all fractions). Analytical methodologies: four-acid-HBr/ICP mass spectroscopy (Ag, As, Bi, Co, Cu, Ni, Pb, Se, Te, Zn), lithium borate fusion/ICP optical emission spectroscopy (Al, Ca, Cr, Fe, K, Mg, Mn, Na, P, Sc, Si, Ti), and lithium borate fusion/ICP mass spectroscopy (Ce, Dy, Er, Eu, Gd, Ho, La, Lu, Mo, Nb, Nd, Pr, Sm, Sn, Sr, Tb, Th, Tm, $U_3O_8$, W, Y, Yb, Zr). * Total fluorine and gold fire assay data was generated at the laboratories of Bureau Veritas (Adelaide). Minimum limits of detection: F 0.004%, Al 0.01%, Ca 0.01%, Fe 0.01%, K 0.01%, Mg 0.01%, Mn 0.005%, Na 0.01%, P 0.01%, Si 0.01%, Ti 0.005%, $CO_2$ 0.05%, Au 0.02 ppm, Ag 0.95 ppm, As 5 ppm, Bi 0.01 ppm, Co 0.1 ppm, Cu 1 ppm, Mo 1 ppm, Ni 1 ppm, Pb 5 ppm, Sn 1 ppm, Th 0.05 ppm, $U_3O_8$ 0.5 ppm, W 1 ppm, Zn 1 ppm, Y 0.5 ppm, La 0.02 ppm, Ce 0.5 ppm, Pr 0.05 ppm, Nd 0.1 ppm, Sm 0.05 ppm, Eu 0.05 ppm, Gd 0.05 ppm, Tb 0.02 ppm, Dy 0.05 ppm, Ho 0.02 ppm, Er 0.05 ppm, Tm 0.05 ppm, and Yb 0.05 ppm. I.S.: insufficient sample; not enough for an accurate gold assay.

### *3.2. Mineral Liberation Analysis*

Mineral Liberation Analysis (MLA) is a widely used quantitative automated mineralogy technique, which combines scanning electron microscopy (SEM) with energy-dispersive X-ray spectroscopy (EDS) to characterize mineral grains in terms of mineral species, grain size, shape, associations, and degree of liberation. These characteristics are critical for understanding the role of mineralogy and ore textures in mineral processing (e.g., [38]). In this study, quantitative mineral proportion and association datasets were determined in each of the ten polished blocks at ALS Global, Brisbane, Australia, following procedures outlined in [39]. Data used in this contribution was obtained via the Extended Liberation Back-Scatter (XBSE) method. It was, however, supplemented with grain-based X-ray mapping (GXMAP) to help resolve sericite, $KAl_2(AlSi_3O_{10})(OH)_2$, and K-feldspar. MLA data were not collected on the finest fraction (+C7) because the particle size was below the reliable detection limit of the MLA system. The resolution of the MLA technique (i.e., pixel size) varies with screen size, and error margins on the proportion of each mineral phase are dependent on the concentration of each mineral in each size fraction.

### *3.3. Microanalysis*

After MLA investigation, each polished block was carbon-coated and examined at high magnification on a Quanta 450 scanning electron microscope (SEM) manufactured by FEI (Hillsboro, OR, USA) and housed at Adelaide Microscopy (Adelaide University). High-contrast imaging was performed in back-scattered electron (BSE) mode. The instrument was operated at 10 nA beam current and 20 kV voltage. The built-in energy-dispersive spectrometer (EDS) (Oxford Instruments, High Wycombe, UK) allowed the acquisition of compositional data for particles in the tailings. The EDS method is standardless and the total of all measured concentrations is normalized to 100%, excluding any OH or $H_2O$ present. The carbon coating added for improved conductivity impairs accurate analysis of carbon-containing minerals; however, roughly, analyses containing more than 10–12% C contain structurally bound carbon. Although favourably comparing with electron probe microanalysis for many common minerals, EDS data are normalized to 100% and cannot adequately navigate complex X-ray interferences among, for example, individual HREEs.

## 4. Results

### *4.1. Assay Data*

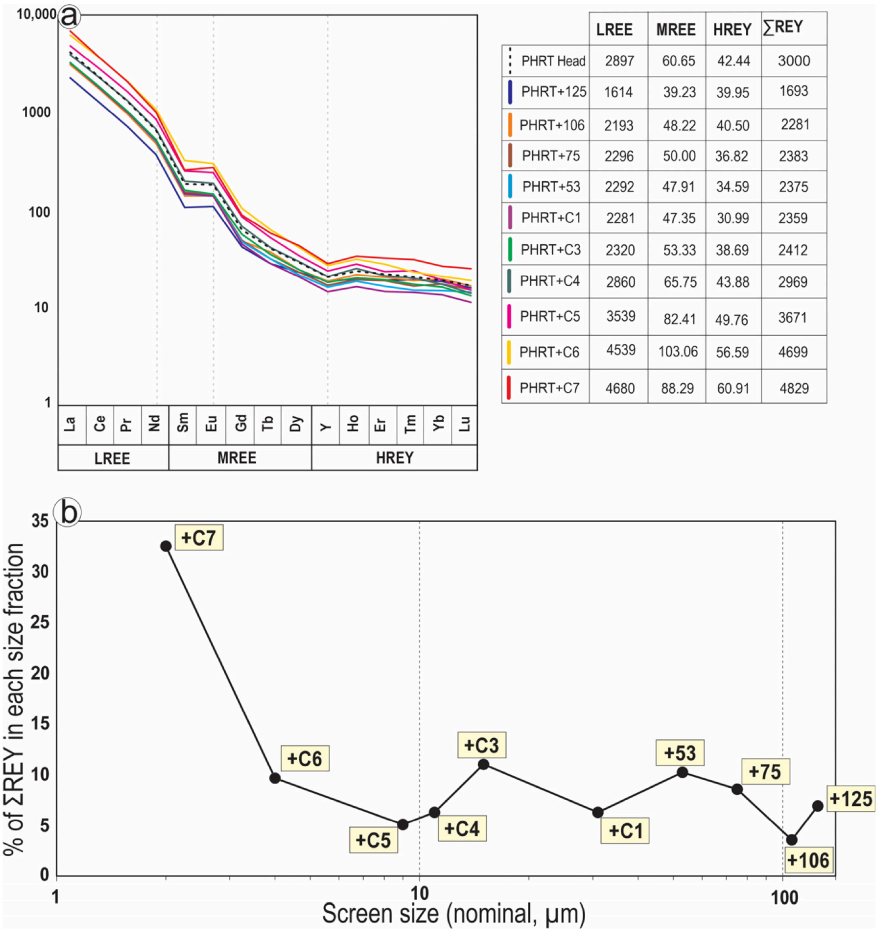
The sample head and each of the ten individual size fractions were assayed commercially for a total of sixty-three elements at the laboratories of Intertek, Adelaide, Australia (with exception of F and Au at Bureau Veritas, Adelaide). Analytical methodologies can be found in the footnote to Table 1. Residual copper is highest in the coarser size fractions.

Chondrite-normalized REE fractionation trends for the ten size fractions and calculated unsized sample (Figure 2a) show subtle variations. The finest fractions (+C6 and +C7) exhibit patterns that are similar in shape to the coarser fractions yet at significantly higher ΣREE concentrations. Fractionation patterns for all size fractions show a steep downwards trend from LREEs to HREEs but are relatively flat across the HREE segment. The enrichment in LREEs (La through Nd) relative to MREEs and HREEs is commensurate with the observations described below. The +125 µm and +C1 fractions display the lowest overall REE concentrations. All size fractions display a clear positive Eu anomaly and a barely perceptible negative Y anomaly.

Figure 2b clearly demonstrates the relative significance of the finest fraction as a major REE host, accounting for >50% of the total REEs in the sample.

The concentration of $U_3O_8$ reaches a maximum of 136 ppm in the very fine (+C7, +2 µm) fraction (Figure 3). The adjacent fine fractions (+C3 to +C6, 4–31 µm) exhibit slightly

lower concentrations, whereas the +C1 fraction (+31 µm) also shows a relatively elevated value of 121 ppm. This anomaly is attributable to separation during cyclosizing being dependent on density, and to some extent also particle shape, as well as particle size.




| | LREE | MREE | HREY | ΣREY |
|---|---|---|---|---|
| PHRT Head | 2897 | 60.65 | 42.44 | 3000 |
| PHRT+125 | 1614 | 39.23 | 39.95 | 1693 |
| PHRT+106 | 2193 | 48.22 | 40.50 | 2281 |
| PHRT+75 | 2296 | 50.00 | 36.82 | 2383 |
| PHRT+53 | 2292 | 47.91 | 34.59 | 2375 |
| PHRT+C1 | 2281 | 47.35 | 30.99 | 2359 |
| PHRT+C3 | 2320 | 53.33 | 38.69 | 2412 |
| PHRT+C4 | 2860 | 65.75 | 43.88 | 2969 |
| PHRT+C5 | 3539 | 82.41 | 49.76 | 3671 |
| PHRT+C6 | 4539 | 103.06 | 56.59 | 4699 |
| PHRT+C7 | 4680 | 88.29 | 60.91 | 4829 |

**Figure 2.** (**a**) Chondrite-normalized REE fractionation trends and summary of REE concentration data (in ppm) for different size fractions and head sample. Chondrite values after [40]. LREE: La, Ce, Pr and Nd; MREE: Sm, Eu, Gd, Tb and Dy; HREE: Ho, Er, Tm, Yb, Lu and Y. (**b**) Partitioning of ΣREY across the size fractions.

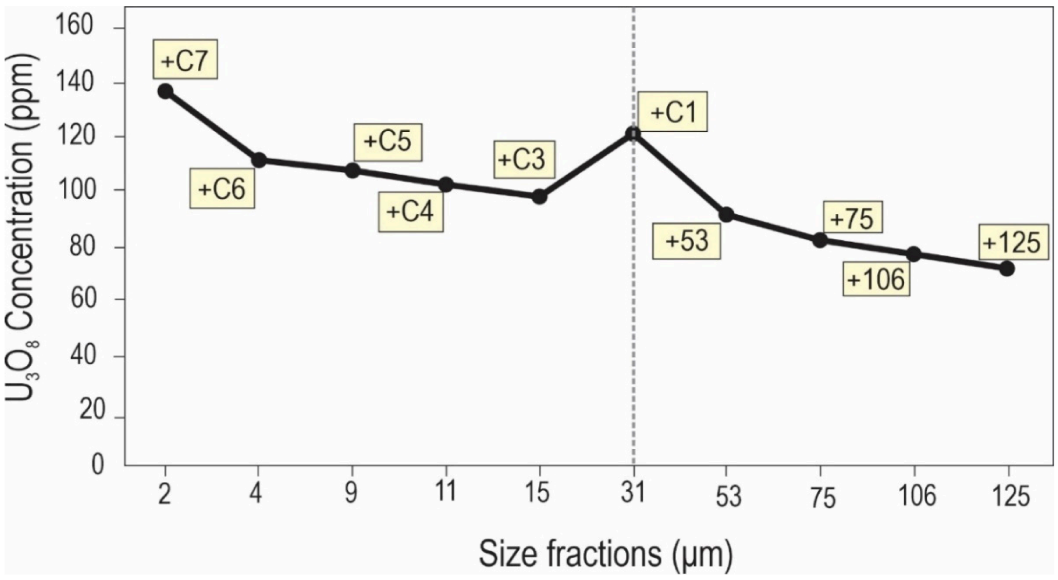



**Figure 3.** Variation in $U_3O_8$ concentration (ppm) across different size fractions.

### *4.2. Mineral Liberation Analysis Data*

In the coarse size fractions, REE-bearing minerals show a strong association with gangue minerals, across all size fractions. Hematite is the most common gangue mineral associated with REE minerals, indicating its persistent textural relationship with REE phases irrespective of grain size. Second in importance is quartz ($SiO_2$), with which up to 40% of florencite, (Ce, La, Nd, Ca, Sr)(Al, Fe)$_3$($PO_4$)$_2$($OH$)$_6$, and bastnäsite, (Ce, La, Nd, Pr, Ca) ($CO_3$)F, is associated in some fractions. Additional, albeit minor, gangue hosts for REE phases include sericite and chlorite.

Across the three coarsest fractions (+125 µm, +106 µm, and +75 µm; Supplementary Materials Figure S1), xenotime, Y($PO_4$), shows a particularly strong association with carbonate minerals, with proportions reaching up to approximately 25%. Xenotime is the sole REE-bearing mineral to exhibit such a strong association with carbonates; the other REE minerals show only minor or no association with carbonates.

The degree of liberation of REE minerals is generally low in the coarser size fractions, not exceeding 10% in some cases, such as monazite, (Ce, La, Nd, Fe, Ca) $PO_4$, and xenotime in the +125 µm and +106 µm fractions. However, synchysite, Ca (REE, Y, Fe, Th, U) ($CO_3$)$_2$F, and florencite show the highest degree of liberation in the coarse and medium fractions (+53 µm, +C1 and +C3; Supplementary Materials Figure S2) with proportions that can reach up to 59.52% and 52.31% for synchysite and florencite, respectively.

In contrast, the finest size fractions (+C4, +C5, and +C6) contain a high proportion of liberated REE minerals (Figure 4). Liberation increases progressively with decreasing particle size and exceeds 90% in the +C6 fraction. Association with gangue minerals is only minor in these fine fractions. Instead, there is a strong association with other REE-bearing minerals (up to 38.65% in some cases, e.g., xenotime).

Among the different REE minerals, monazite and bastnäsite show the highest degrees of liberation (Figure 4) whereas xenotime exhibits the lowest proportions of liberated grains (only 18.74% in the +C4 fraction and 68.48% in the +C5 fraction). In the finest fraction (+C6) (Figure 4), liberation of xenotime reaches 93.48%, comparable with that of other REE minerals.

### *4.3. REE Mineral Size-Dependent Variation*

A plot of particle size and percentage of exposed surface area for different REE-bearing minerals (Figure 5) reveals the expected inverse relationship between the two variables. Distinct patterns among individual REE minerals indicate a strong mineralogical control, where discrete REE phases show greater surface exposure than those occurring as inclusions or intergrowths within gangue. These textural relationships are consistent with the SEM-EDS observations detailed below and carry important implications for REE liberation and thus potential recovery. While fine grinding enhances surface exposure, REEs hosted in complex mineral matrices may remain partially inaccessible. Figure 5 shows that the proportion of surface exposure is highest in the very fine size fraction for all REE minerals, as expected, and decreases markedly in the +4 to −15 µm size range (+C6 to +C4).

Xenotime and APS minerals (woodhouseite, goyazite, svanbergite, etc., loosely combined as phases of the 'crandellite group' in the MLA software library, and typically containing a few wt.% REEs) display the lowest overall degrees of surface exposure among the REE minerals (Figure 5). Synchysite shows relatively low surface exposure in the fine fractions but exhibits a progressively fluctuating increase toward coarser sizes, with a pronounced peak in the +106 µm fraction. In contrast, florencite and apatite record the highest surface exposure in the fine size fractions and, consistent with other REE minerals, display a fluctuating decrease in exposure with increasing particle size.

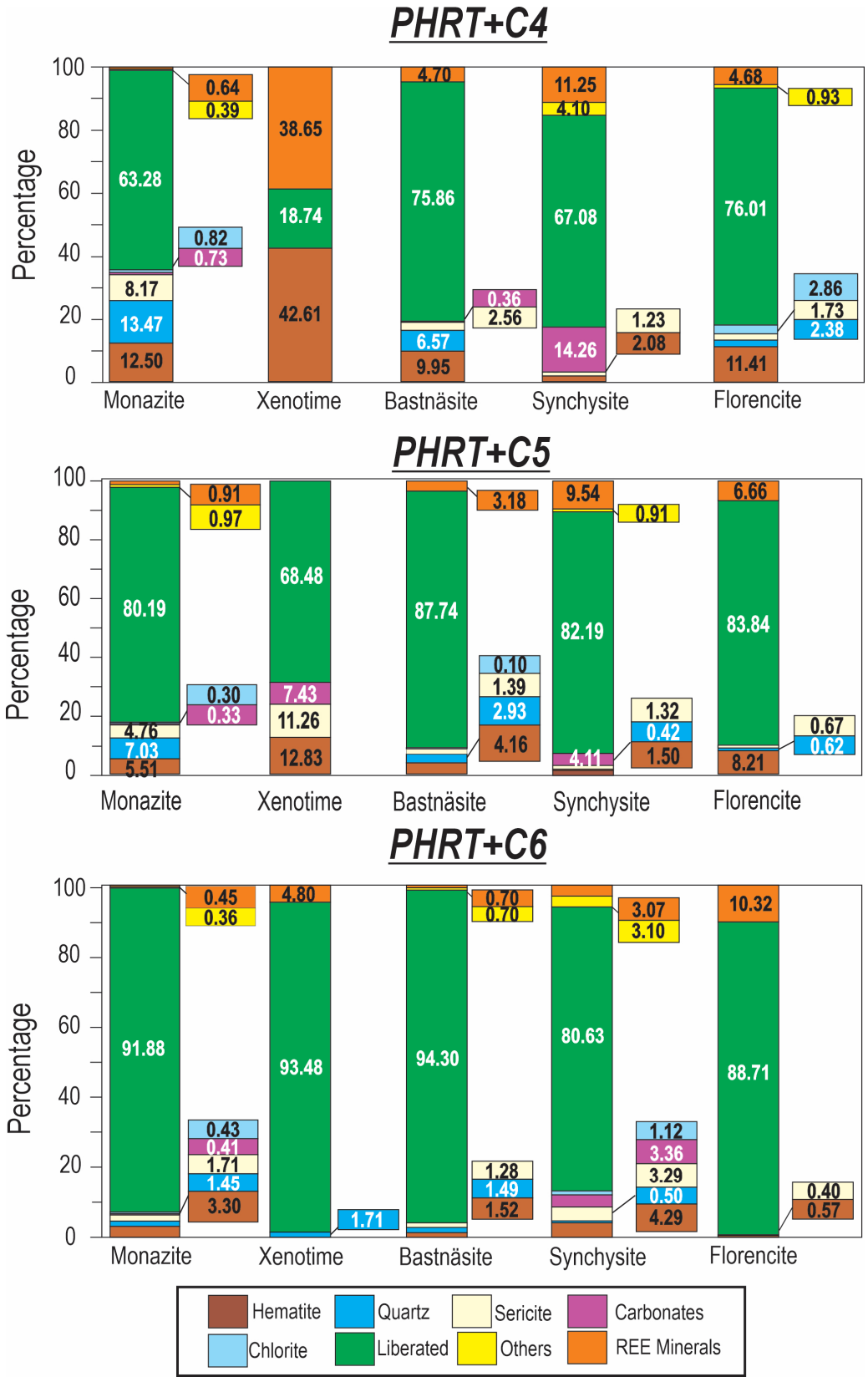



**Figure 4.** Bar charts showing the associations of five REE minerals in three fine size fractions. For the purposes of this figure, all chlorite-group minerals (both Fe- and Mg-rich) are grouped together. 'Carbonates' represents calcite + dolomite + siderite + ankerite. 'Hematite' is all Fe-oxides. See text for additional explanation. 'REE minerals' represents the total of monazite + xenotime + bastnäsite + synchysite + florencite + APS minerals (Ca-Sr-dominant aluminum-phosphate–sulphate minerals of the alunite supergroup).

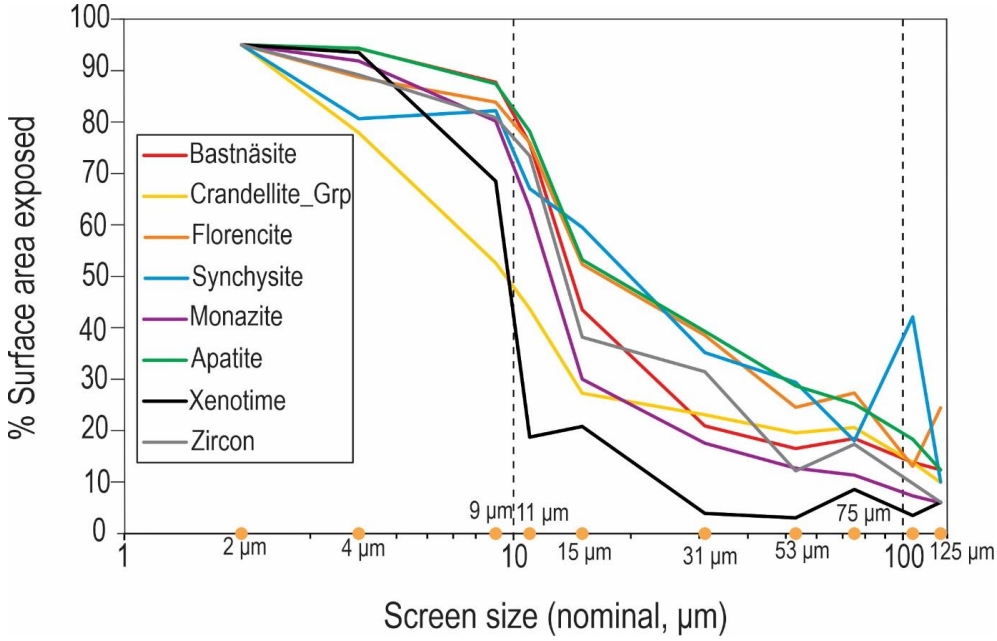



**Figure 5.** Comparison of particle size vs. % surface area exposed for different REE minerals. Note the marked difference between parameters for monazite and xenotime (little surface exposure of particles over 10 µm), and those for florencite, synchysite and bastnäsite.

### *4.4. Rare Earth Mineralogy*

The tailings contain several dozen different minerals (Supplementary Materials Table S1), including a diverse ecology of REE- and U-bearing species. These display a range of mutual, and often complex, replacement relationships. Alongside discrete REE minerals, rare earths are also detected at trace to minor levels within zircon $ZrSiO_4$, uraninite (ideally $UO_2$) and coffinite, $USiO_4 \cdot nH_2O$.

### *4.5. REE Phosphates*

Imaging and MLA data indicate that monazite is the most abundant REE mineral. Monazite commonly occurs as relatively coarse grains, reaching approximately 10–20 µm in size, and is typically associated with gangue minerals. The euhedral to subhedral monazite aggregate in Figure 6a, for example, is enclosed within a chlorite–quartz matrix. Higher-magnification imaging reveals that this monazite aggregate has a structure encompassing micro-pores. Monazite also appears enclosed (i.e., locked) within assemblages of hematite–sericite, where it also displays visible micro-fractures and pores (Figure 6b,c). Disseminations of monazite, 1–5 µm in size, are also commonly observed within gangue minerals, such as hematite (Figure 6d) and sericite. Other textures involving monazite are observed, such as the 'massive' aggregate of microcrystals in association with hematite and quartz (Figure 6e).

EDS analysis reveals that only monazite-(Ce) is present. Contents of La always exceed those of Nd in all grains of monazite we have analyzed (11.0–25.8 wt.% La, Nd never exceeding 9 wt.%). There is a marked inverse correlation between the two elements in which samples with greater La (e.g., 25.8 wt.% La) contain the least Nd (3.1 wt.%). Traces of other LREEs are noted in monazite, including samarium (Sm), praseodymium (Pr), Fe and Ca, but no measurable HREEs.

Florencite is the second most abundant REE phosphate. Two species are observed: florencite-(Ce), the more abundant of the two, and florencite-(La). Various textures of florencite are noted, where well-crystallized grains form aggregates with sericite, quartz and/or hematite (Figure 6f,g). Florencite also infills particles containing bornite (Figure 6h).

Florencite-(Ce) contains measurable Nd (up to 3.1 wt.%), whereas Nd is not detected in florencite-(La). Alongside LREEs, strontium (Sr) is the most common trace element in florencite (typically 1–3.4 wt.%).

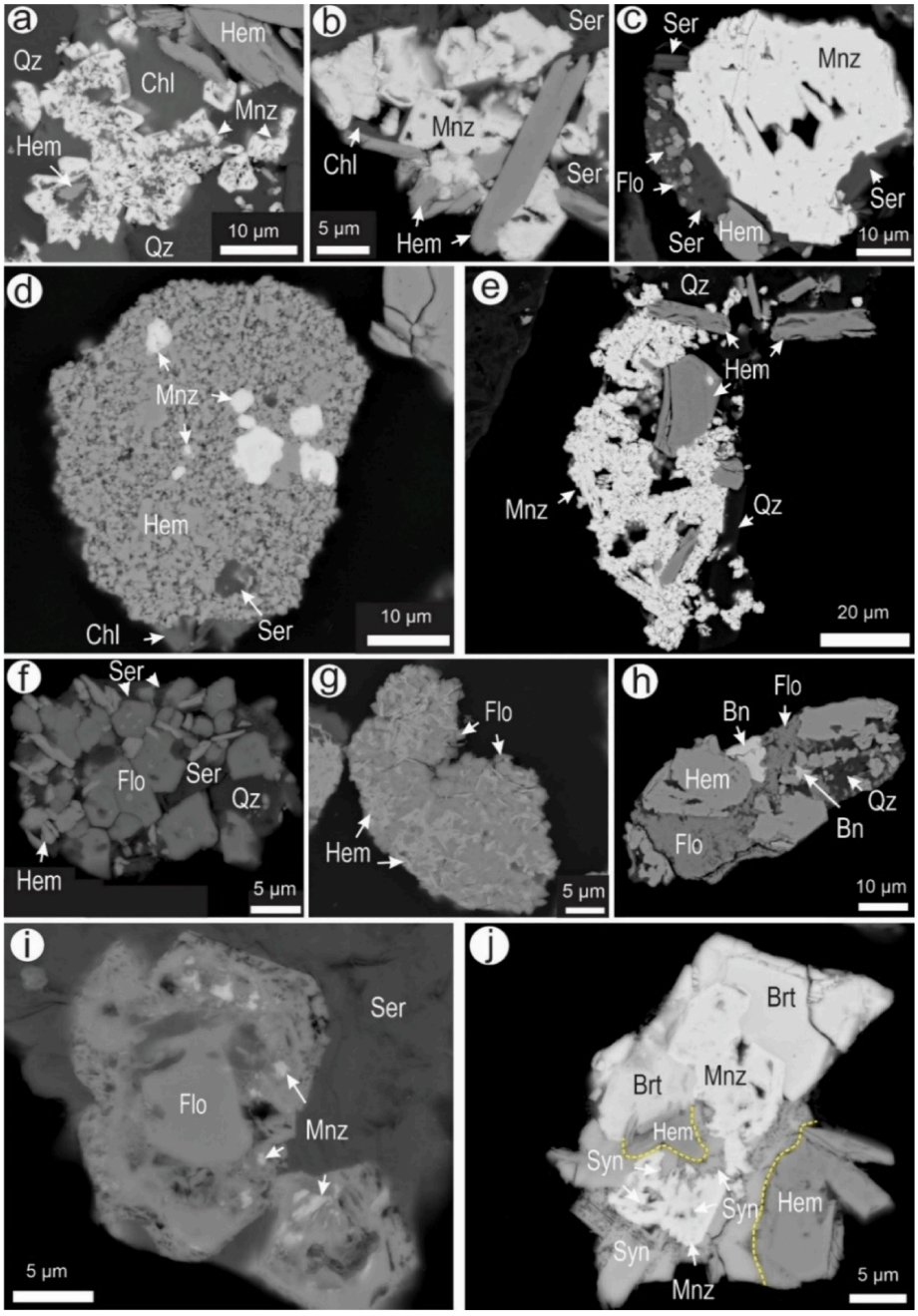



**Figure 6.** BSE images showing different textural aspects of monazite (Mnz), florencite (Flo), and their mutual replacement relationships. (**a**) Monazite grains within a polymineralic particle. (**b**) Monazite grains locked within an assemblage of hematite (Hem), sericite (Ser), and chlorite (Chl). (**c**) Polymineralic particle hosting relatively coarse fractured monazite. (**d**) Disseminations of monazite within fine-grained hematite. (**e**) Massive aggregate of microcrystalline monazite within hematite–quartz (Qz). (**f**) Well-crystallized florencite associated with hematite, sericite and quartz. (**g**) Fine aggregate of florencite associated with acicular hematite. (**h**) Mixed particle showing fine-grained florencite associated with hematite, bornite (Bn) and quartz. (**i**) Monazite replaced by florencite and preserved only as relicts within a matrix of sericite. (**j**) Replacement of monazite by synchysite (Syn) in a particle also containing baryte (Brt) and hematite. Yellow lines indicate boundaries between minerals that are not otherwise easily distinguishable.

Monazite exhibits incomplete replacement by other REE minerals. Notably, florencite is seen to commonly replace monazite, with remnants of the original monazite preserved as relict grains (Figure 6i). Although the phenomenon appears rare, monazite is also observed in the early stages of replacement by synchysite (Figure 6j).

### *4.6. REE Fluorocarbonates*

REE fluorocarbonates are observed in all size fractions, although generally subordinate to REE phosphates. Several species are noted. REE fluorocarbonates can be represented by the general formula (REE,Ca)($CO_3$)Z, where Z represents a site that may be occupied by fluorine (F), chlorine (Cl), or hydroxyl (OH) anions [41].

Among the REE fluorocarbonates, bastnäsite, commonly associated with quartz, hematite and sericite, displays the broadest range of textures including euhedral lamellae, infilling hematite, or randomly oriented aggregates (Figure 7a–d). Disseminated, acicular crystals of bastnäsite occur within hematite–chlorite–quartz associations (Figure 7e). Bastnäsite also appears as intensely fractured polymineralic particles, ~20 μm in size, in which the micro-fractures are infilled by bornite (Figure 7f).

EDS analysis indicates that bastnäsite-(Ce) is the dominant species, and bastnäsite-(La) is subordinate. Bastnäsite-(Ce) is generally richer in La than Nd. In most analyses, La is relatively high, whereas Nd remains low. Bastnäsite-(La), on the other hand, is Nd-deficient, never exceeding 4 wt.%. Although bastnäsite is primarily an LREE mineral, small amounts of HREEs, notably Y, are detected yet remain below 1.5 wt.%. Bastnäsite also contains measurable amounts of other LREEs, including Sm and Pr, as well as traces of Fe and Ca.

Lamellar aggregates of bastnäsite and synchysite appear generally fractured, exhibiting textures indicative of partial or advanced replacement. In most, though not all, cases (e.g., Figure 8a,b), textures are suggestive of partial replacement of bastnäsite by synchysite, with the former only preserved as corroded relicts (Figure 8b). REE fluorocarbonates are commonly intergrown with one another and are associated with sericite, hematite, and quartz (Figure 8c–g). These intergrowths typically range from 5 to 20 μm in size. Bastnäsite is also observed to form lamellae parallel to synchysite within quartz–hematite associations or even overgrow the synchysite (Figure 8c). Bastnäsite also occurs as fine acicular crystals oriented in multiple directions within synchysite, which is in turn enclosed by chlorite (Figure 8g). Synchysite-(Ce) is the only species of synchysite identified. Like bastnäsite-(Ce), synchysite-(Ce) is richer in La than Nd; however, it typically contains greater concentrations of Nd than coexisting bastnäsite whenever the two minerals appear together. Synchysite also contains measurable amounts of other REEs, including Sm and Pr, as well as minor Y.

More rarely, parisite, $Ca(Ce,La)_2(CO_3)_3F_2$, is observed as particles displaying lamellar intergrowths with bastnäsite and in association with quartz (Figure 8h,i). In such cases, internal textures suggest an early stage of replacement of bastnäsite by parisite, rather than co-crystallizing relationships between the two REE fluorocarbonates. Micro-fractured parisite occurs as ~10 μm sized particles and contains small inclusions of bastnäsite (Figure 8j), which are likely surviving relicts from incomplete replacement.

Of direct relevance for understanding cycles of remobilization–recrystallization and the relative age of REE minerals and overprinting events at Prominent Hill is the observation that the F content of bastnäsite is systematically higher (roughly double) than that of the replacive Ca-rich fluorocarbonate (synchysite or parisite) whenever they are seen to spatially coexist (e.g., Figure 8h–j). Given that Cl and OH occur in the Z site alongside F, and no measurable Cl is recorded, the inference is that the OH content of the Ca-rich fluorocarbonate must be higher. Assuming full occupancy of the Z site, this interpretation would, however, require independent verification, e.g., via in situ analysis of OH content.

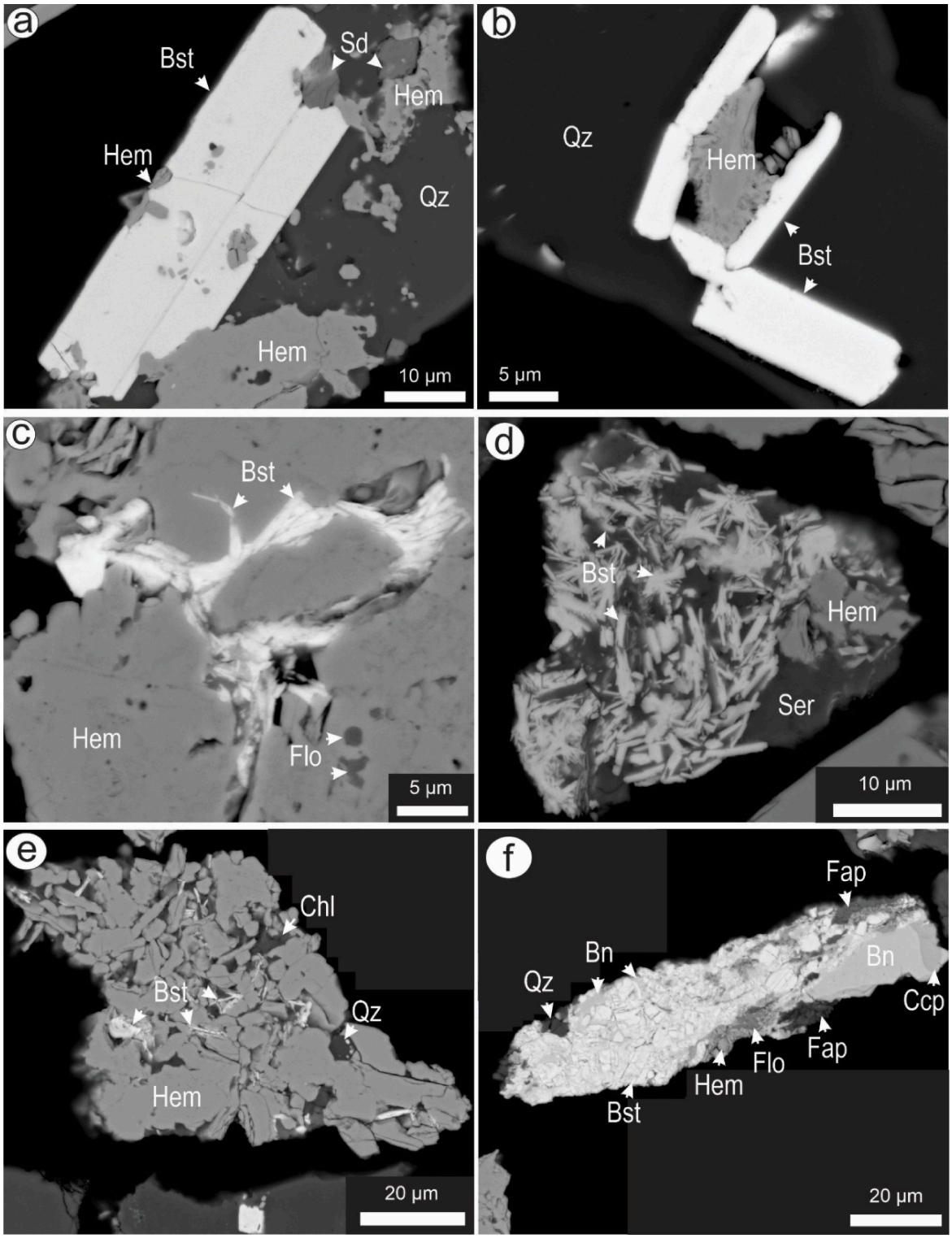



**Figure 7.** BSE images showing textural aspects of bastnäsite (Bst) and its association with various gangue and ore minerals. (**a**,**b**) Bastnäsite enclosed in hematite (Hem) and quartz (Qz). (**c**) Microveinlet of bastnäsite within fine-grained hematite. (**d**) Randomly oriented bastnäsite within assemblage of sericite (Ser) and hematite (Hem). (**e**) Acicular bastnäsite disseminated within fractured hematite. (**f**) Polymineralic particle showing bastnäsite fractured and replaced by bornite (Bn). Sd—siderite; Flo—florencite; Chl—chlorite; Fap—fluorapatite; Ccp—chalcopyrite.

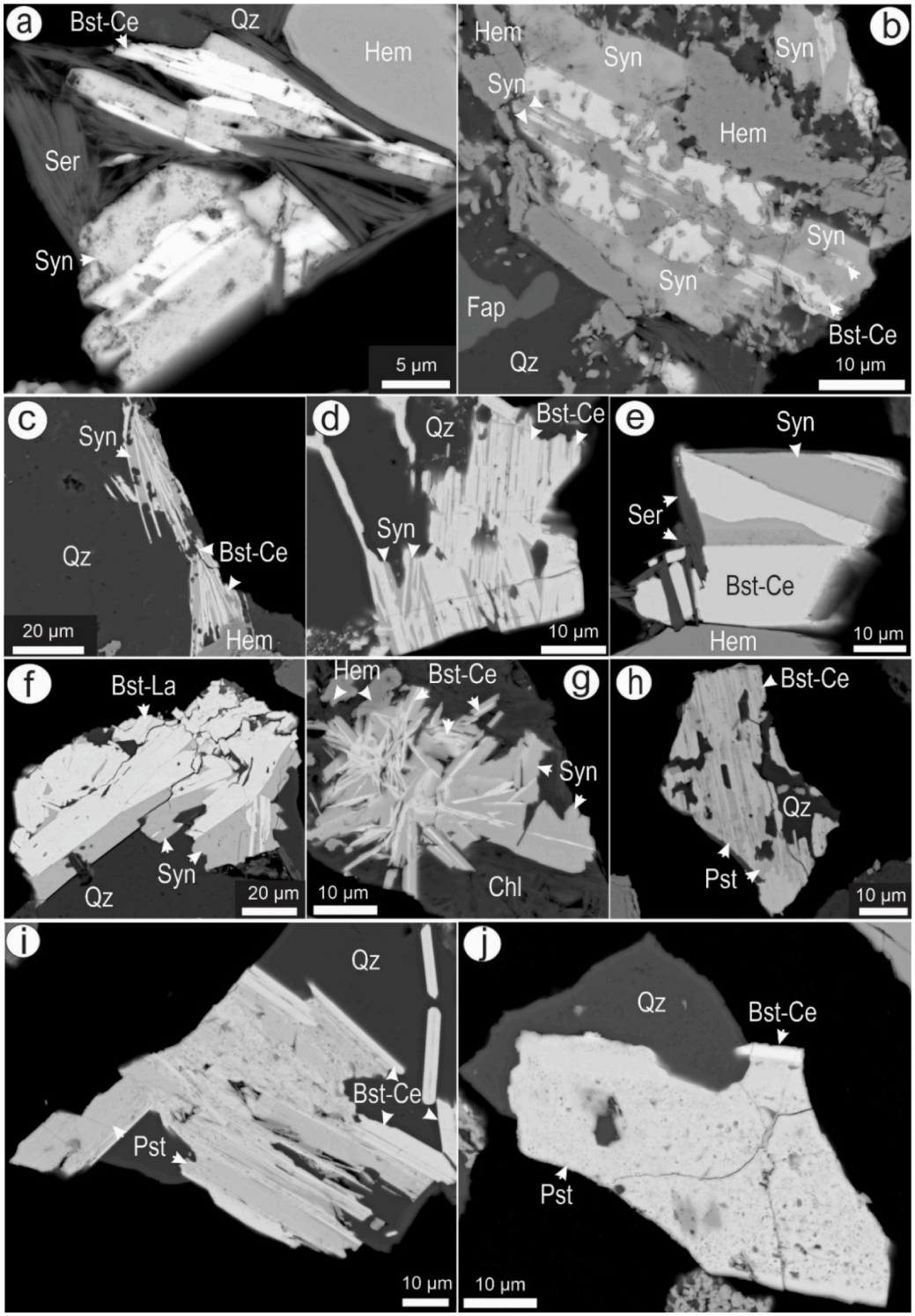



**Figure 8.** BSE images showing different textures of REE-fluorocarbonate minerals and their mutual intergrowths. (**a**,**b**) Incomplete replacement of bastnäsite-Ce by synchysite (Syn). Fap—fluorapatite. (**c**) Lamellar bastnäsite-Ce intergrown with synchysite and enclosed within quartz. (**d**) Intergrowth of synchysite-Ce with bastnäsite-Ce enclosed within quartz. (**e**) Intergrowth of bastnäsite-Ce and synchysite-Ce (Syn) associated with sericite (Ser) and hematite (Hem). (**f**) Micro-fractured intergrowth of bastnäsite-La (Bst-La) and synchysite-Ce associated with quartz. (**g**) Needle-like bastnäsite-Ce intergrown with synchysite-Ce and enclosed within chlorite (Chl). (**h**,**i**) Bastnäsite-Ce (Bst-Ce) intergrown with parisite-Ce (Pst) and associated with quartz (Qz). (**j**) Relatively coarse, homogeneous parisite with marginal bastnäsite. Parisite appears light grey on BSE images, consistent with its lower Ca content relative to synchysite.

### *4.7. Uranium Mineralogy*

Uranium-bearing minerals are observed in all size fractions. Uraninite and coffinite are the most abundant species. Wyartite, $CaU^{5+}(UO_2)_2(CO_3)O_4(OH).7H_2O$, is observed in minor amounts. Uraninite displays a wide range of textures and is associated with different minerals. Uraninite is widely noted as micro-inclusions with a characteristic cubic cross-section, a few µm in diameter, within hematite (Figure 9a,b). In some cases, uraninite occurs as clustered inclusions, typically just 1–5 µm in size within hematite (Figure 9c,d). EDS data shows uraninite to contain highly variable contents of Pb (between 1.3 and 18.4 wt.%). In addition to Pb, EDS analyses reveal the presence of REEs in uraninite, notably Ce, Nd, Dy and Y, and minor Th, as well as Fe (from hematite matrix), Ca and Mn (alteration?). Monazite grains also host tiny inclusions of uraninite (Figure 9e).

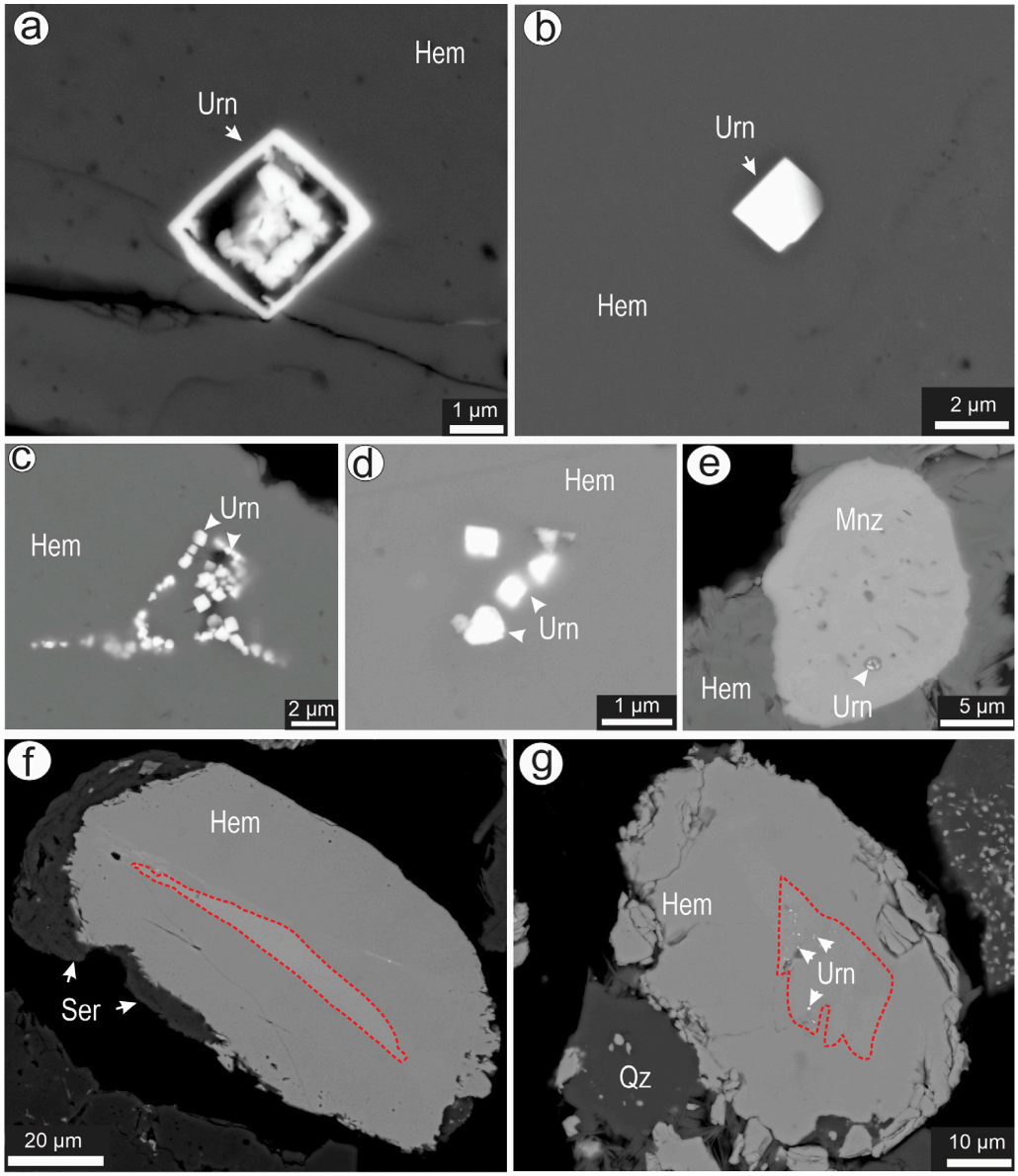



**Figure 9.** BSE images illustrating the distribution of uraninite (Urn) within hematite (Hem). (**a**,**b**) Micro-inclusions of uraninite with cubic cross-section within hematite. (**c**,**d**) Dense concentrations of uraninite within hematite. (**e**) Tiny uraninite inclusion enclosed within monazite (Mnz). (**f**) Zoned hematite associated with sericite (Ser) and highlighted red zone is rich in U (+Pb). (**g**) Zoned hematite associated with quartz (Qz) and highlighted red zone is rich in U with fine inclusions of uraninite.

High-contrast BSE imaging (Figure 9f,g) shows that some hematite grains are compositionally zoned, in which the brighter and apparently homogeneous zones are relatively enriched in U (reaching several wt.%) and, in some cases, also measurable Pb (highlighted red zone in Figure 9f). EDS analyses reveal contents of U as high as 4.5 wt.%. In other cases, high-magnification imaging of hematite shows the U as finely disseminated uraninite nano-inclusions (highlighted red zone in Figure 9g). Clustered inclusions of uraninite in hematite are a common feature throughout the South Australian IOCG ores (e.g., [42]). They are the product of U release during recrystallization of the host hematite, as well as healed micro-fractures that have trapped circulating (remobilized) uranium.

Uranium carbonates, particularly wyartite, are commonly associated with uraninite. Thin seams of wyartite enclose relict uraninite within larger multiphase (hematite–bornite–chlorite) particles. Wyartite also typically occurs as fine, sub-μm-scale intergrowths within coarser "cobweb" uraninite (Figure 10a–c). The presence of Ca and Mn in our EDS analyses of uraninite suggests early-stage incipient replacement of uraninite by very fine-grained wyartite. Conspicuous textures like these, displaying a rhythmic intergrowth of uraninite with Cu-Fe sulphides, are described in Olympic Dam and were interpreted to represent a replacement type of uraninite ("third class of grains"; [43]), formed late relative to the small, euhedral grains like those in Figure 9a–d. Distinct from the Olympic Dam uraninite is the presence at Prominent Hill of wyartite associated with cobweb uraninite that exhibits lower Pb concentrations. Unlike uraninite, which it replaces, the wyartite contains no detectable REEs. EDS analysis of other wyartite in different fractions reveals measurable REE (Ce and Y reaching almost 2 and 3 wt.%, respectively). Traces of Fe, Mg, and Mn are also noted.

Marginal replacement of uraninite by bornite is also observed. In such cases (Figure 10d), the marginal uraninite area (darker on the BSE image; no Pb, elevated Ca, Si, and slightly increased Y) is compositionally distinct from the remainder (brighter on the BSE image; measurable, relatively low Pb, generally <5 wt.%, with minor Ce and Y). The composition of the darker regions in Figure 10d is suggestive of a possible early formation of coffinite–xenotime as a replacement of uraninite. Coffinite (Figure 10e–h) forms a matrix enclosing finely disseminated uraninite, suggesting either incomplete replacement of uraninite by coffinite or, alternatively, formation of "new" uraninite following partial decomposition of coffinite. These textures are observed in polymineralic particles 5 to 10 μm in size. Associated minerals include quartz, hematite, sericite and $TiO_2$ (rutile, possibly also anatase). In addition, liberated grains of coffinite preserving uraninite relicts are observed. Coffinite also occurs as micro-veinlets within quartz.

EDS analysis indicates that coffinite is a carrier of several minor and trace elements, including Ca and Fe, as well as a few wt.% REEs (notably Nd and Ce, although not exceeding 2.2 wt.% and 2.0 wt.%, respectively). Relatively high concentrations of yttrium (Y) are, however, detected (1.6–5.6 wt.%). We note, however, an absence of phosphorus (P) in coffinite, a feature often taken, along with elevated Y, to indicate coffinite–xenotime solid solution. Phosphorus is only detected within "pure" coffinite, in which uraninite relicts are absent. This discrepancy hints at the correctness of the interpretation involving incomplete "coffinitization" of uraninite.

EDS data indicates that both zircon, $ZrSiO_4$, and xenotime-(Y), $YPO_4$, are minor hosts for U (<1 wt.%).

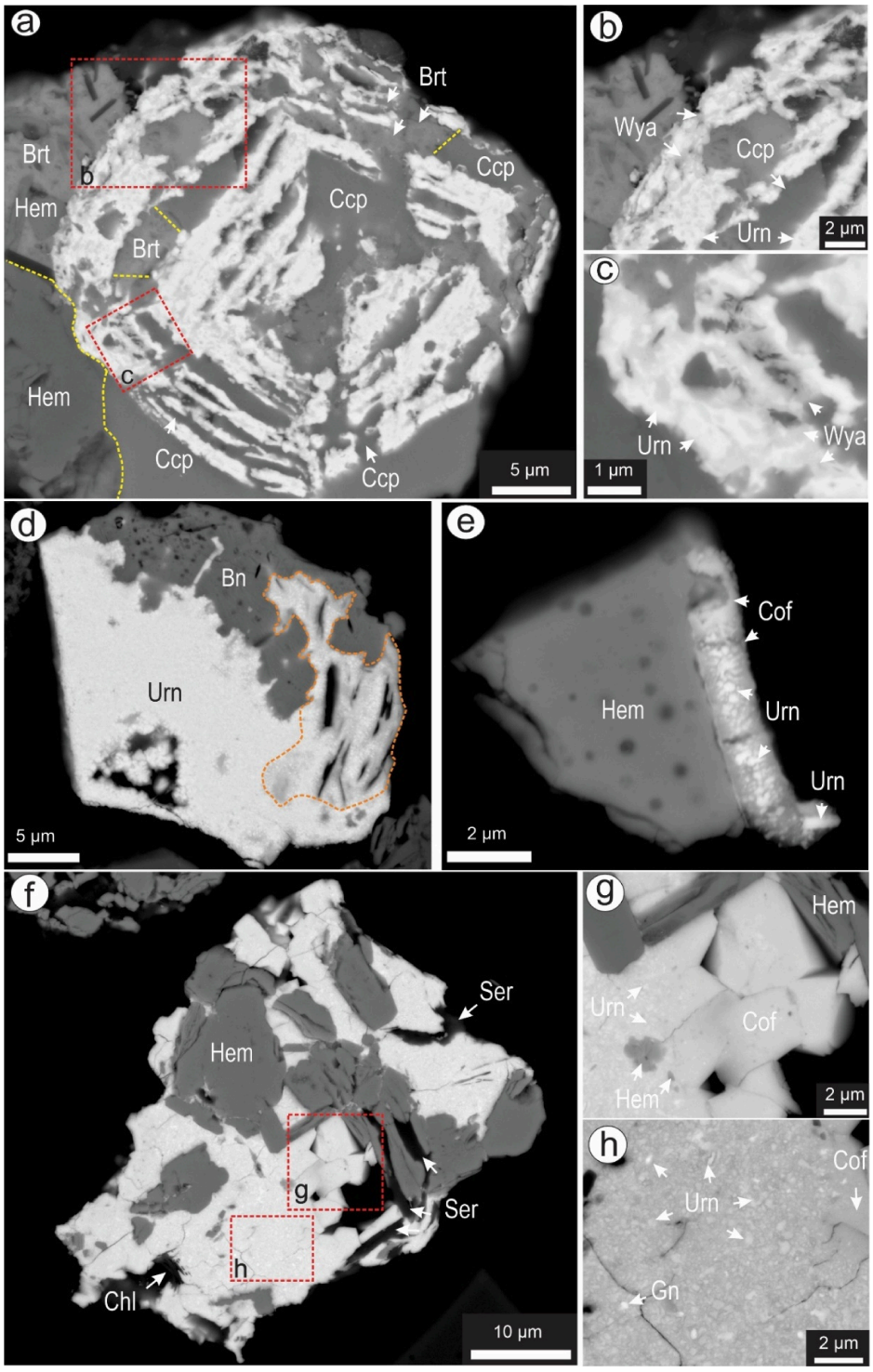



**Figure 10.** BSE images of polymineralic particles containing U-minerals and associated replacement textures. (**a**) Cobweb uraninite displaying rhythmic core-to-margin intergrowths of uraninite (Urn), chalcopyrite (Ccp) and Fe-rich baryte (Brt). Yellow lines indicate mineral boundaries otherwise not easily distinguishable. (**b**,**c**) Details of two specific areas within the cobweb uraninite in (**a**) showing replacement by wyartite. (**d**) Liberated particle showing bornite (Bn) intergrowths with uraninite. The orange zone highlights a darker area that exhibits a subtle deviation from the typical uraninite composition. (**e**) Uraninite relicts preserved within coffinite (Cof) matrix. (**f**) Particle showing replacement of uraninite (Urn) by coffinite in association with hematite (Hem), chlorite (Chl) and sericite (Ser). (**g**) Detail from (**f**) showing well-crystallized coffinite alongside incomplete replacement of uraninite, which is preserved as µm-scale relicts. (**h**) Detail from (**f**) showing uraninite relicts within matrix of coffinite. Gn—galena; Qz—quartz.

### *4.8. Other Minerals*

#### 4.8.1. Zircon

Zircon displays a range of morphologies, textures and associations, in part as a result of presumed diverse origins, igneous, detrital, hydrothermal, and possibly metamorphic, but also because of superimposed alteration and radiation damage. Micro-fractured, fine-grained zircon appears together with small grains of hematite and sericite, typically around 10 μm in size (Figure 11a). In most cases, two compositionally distinct zones are clearly visible in BSE images (Figure 11b–d). Zircon is metamict, commonly highly fractured, and may host tiny inclusions of monazite (Figure 11e). Zircon is also associated with monazite (Figure 11f).

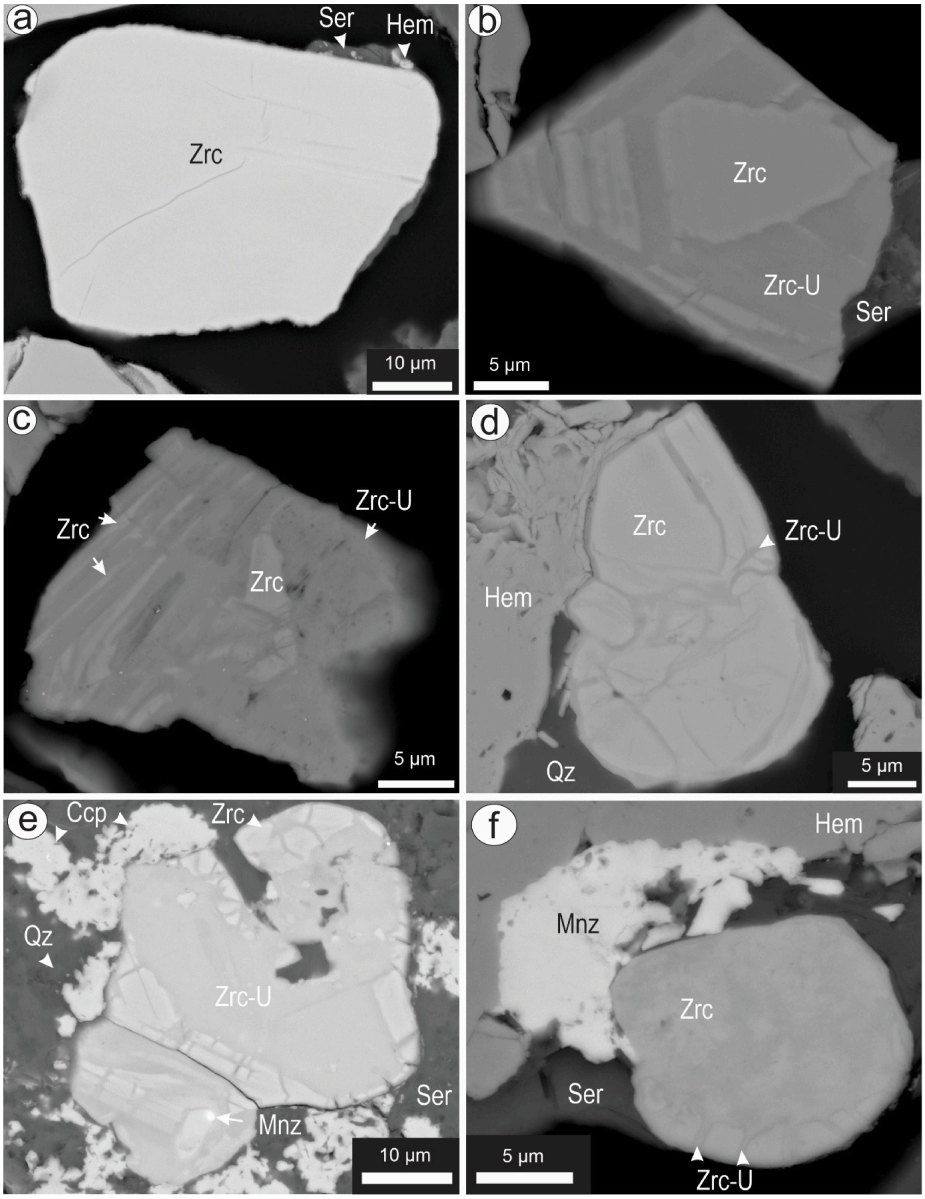



**Figure 11.** BSE images illustrating various textures involving zircon (Zrc). (**a**) Micro-fractured zircon associated with sericite (Ser) and hematite (Hem). (**b**,**c**) Zircon displays two compositionally distinct domains. Pale-grey zones represent less-altered zircon, whereas the dark-grey zones (Zrc-U) contain various non-formula elements, including U, Y, Ca, and Fe. (**d**) Zircon grain enclosed within quartz (Qz) and hematite (Hem). (**e**) Partially altered zircon in association with chalcopyrite (Ccp) and enclosed within an intergrowth of quartz and sericite. (**f**) Zircon associated with monazite (Mnz) and enclosed within sericite–hematite (Hem).

Aside from Hf, common in zircon, the dark zones on the images in Figure 11 contain various non-formula elements, including U (up to 12.4 wt.% in some cases). Detected REEs include Y, Nd and Ce, reaching up to 8.7 wt.%, 1.4 wt.%, and 1.4 wt.%, respectively. Altered zircon also hosts Th, Ca, Al, and Fe. Less-altered zircon (light-grey zones on BSE images, Figure 11) contain only Fe and Hf as impurities. Scandium (Sc) is also noted within zircon, the only mineral containing measurable concentrations of this element within the dark zones. The partially amorphous nature of metamict zircon reported from these ancient rocks [29], together with the presence of micro-fractures, provides effective pathways for fluid infiltration and alteration, which leads to significant changes in its chemical composition, including incorporation of several non-formula elements [29].

#### 4.8.2. Cu-(Fe) Sulphides and Associated Ore Minerals

Cu-(Fe) sulphides are intergrown with each other, notably forming 'basket weave' textures between bornite ($Cu_5FeS_4$) and digenite ($Cu_9S_5$), often enclosed within gangue minerals such as sericite, chlorite and/or hematite (Figure 12a,b). In addition, Cu-(Fe) sulphides host nanoscale inclusions of trace minerals such as monazite (Figure 12b) or clausthalite (PbSe). According to MLA data, bornite is the most abundant Cu-(Fe) sulphide across all size fractions, except in the +C4 fraction, where chalcopyrite ($CuFeS_2$) is slightly more abundant. Chalcopyrite also occurs as network lamellar intergrowths with bornite and enclosed within chlorite (Figure 12c) or associated with chlorite–sericite. In some cases, chalcopyrite hosts tiny inclusions of clausthalite (Figure 12d). Chalcocite, $Cu_{2-x}S$, where x = 0–0.2, is also present, occurring intergrown with carrollite, $CuCo_2S_4$ (Figure 12e).

Pyrite ($FeS_2$) occurs in several forms; most commonly as intergrowths with covellite, CuS (Figure 12f) or bornite (Figure 12g). Pyrite also appears as framboidal aggregates (Figure 12h) within a matrix of dolomite, $CaMg(CO_3)_2$. Micro-fractured galena (PbS) and sphalerite (ZnS) form small aggregates, ca. 10 μm in size (Figure 12i). Galena also occurs as liberated grains, locally associated with minor hematite along grain boundaries (Figure 12j) as well as associated with bornite or intergrown with chalcocite. EDS analysis reveals the presence of what we infer to be secondary atacamite, $Cu_2(OH)_3Cl$, within bornite–chalcopyrite intergrowths.

Clausthalite is predominantly observed as minute inclusions within Cu-(Fe) sulphides. In some instances, the selenide also occurs as extremely fine grains (<1 μm), enclosed within hematite (Figure 13a) and intergrown with an unidentified Cu-sulphide. Altaite, PbTe, is the only telluride identified, occurring as tiny inclusions in bornite only a fraction of <1 μm in size (Figure 13b). Selenide–telluride assemblages resemble those previously illustrated by Owen et al. [44]. Molybdenite ($MoS_2$) is noted in several size fractions as <2 μm sized disseminations within gangue (quartz, sericite, and fluorapatite) (Figure 13c) but also with a marked association with U-minerals and monazite (Figure 13d). Measurable Co is persistently noted in molybdenite. Scheelite, $CaWO_4$, is the sole tungstate detected, identified as ~1 μm inclusions within hematite (Figure 13e).

Minor volumes of arsenides are represented by safflorite, $(Co,Fe)As_2$, and löllingite, $FeAs_2$. Safflorite occurs as fine grains (<2 μm) within quartz (Figure 13f), enclosing minute inclusion of uranium minerals, probably uraninite. EDS analyses indicate minor Ni (5.4 wt.%) and traces of sulphur (<1 wt.%). Löllingite, on the other hand, is observed only as sub-micron grains (<2 μm) within sericite–quartz association. EDS data reveal the presence of ca. 10 wt.% Co and minor Ni not exceeding 3.4 wt.%. An alloy phase containing Au–Pt–Ag is observed (but could not be identified) as a <1 μm sized inclusion enclosed within a zircon–xenotime intergrowth.

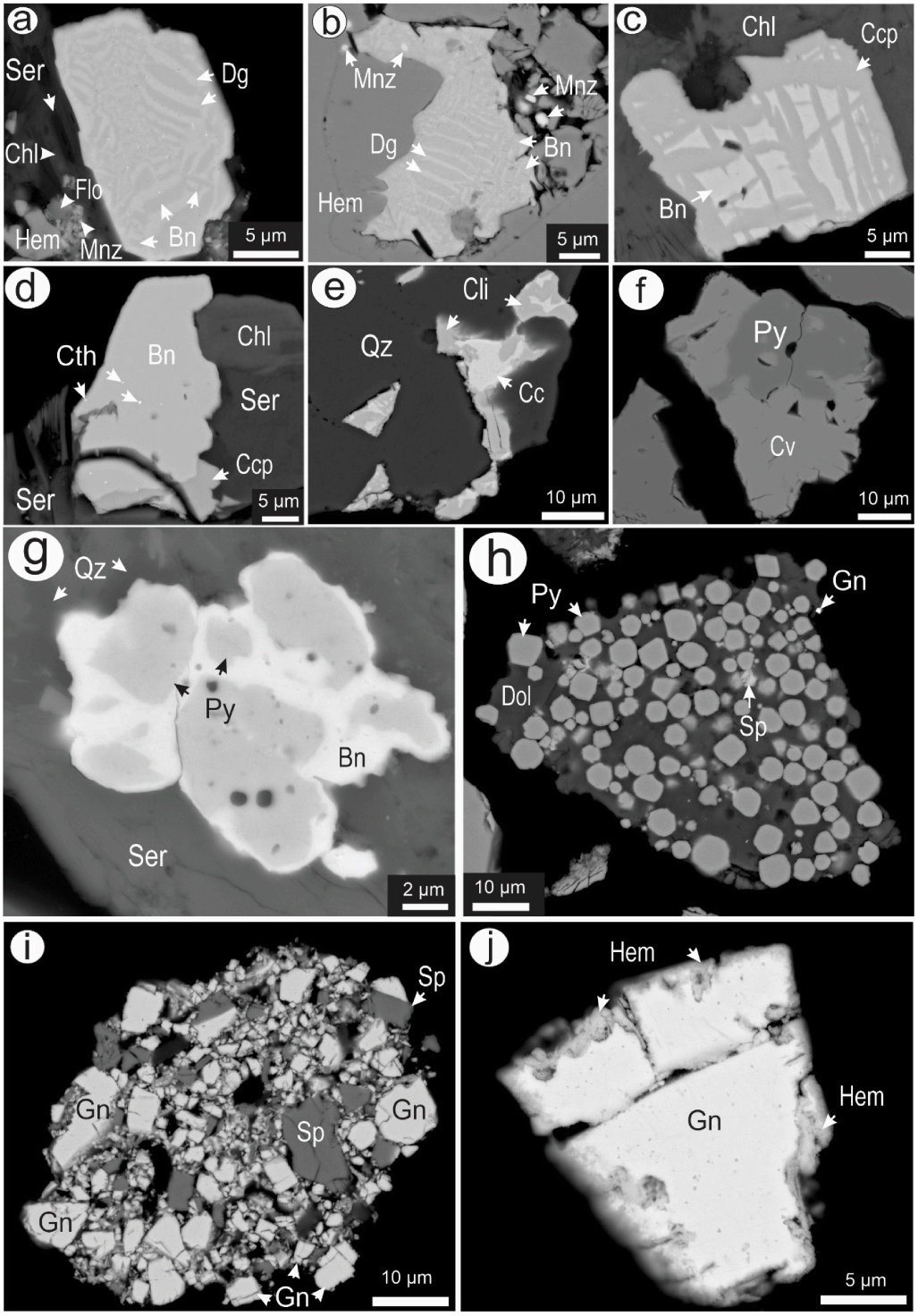



**Figure 12.** BSE images showing aspects of sulphide mineralogy. (**a**) Symplectite between digenite (Dg) and bornite (Bn). (**b**) Digenite–bornite symplectite locked within hematite (Hem) and host to monazite (Mnz). (**c**) Bornite–chalcopyrite (Ccp) intergrowth within chlorite (Chl). (**d**) Bornite–chalcopyrite intergrowth hosting tiny inclusions of clausthalite (Cth) in the bornite associated with chlorite–sericite (Ser). (**e**) Intergrowth of chalcocite (Cc) and carrollite (Cli) within quartz (Qz). (**f**) Liberated grain comprising pyrite (Py) and covellite (Cv). (**g**) Rounded pyrite, corroded and replaced by bornite, within sericite–quartz. (**h**) Framboidal pyrite associated with dolomite (Dol). Note tiny inclusions of galena (Gn) and sphalerite (Sp). (**i**) Particle (agglomerate?) comprising brecciated galena and sphalerite. (**j**) Fractured liberated galena grain surrounded by marginal fine-grained hematite.

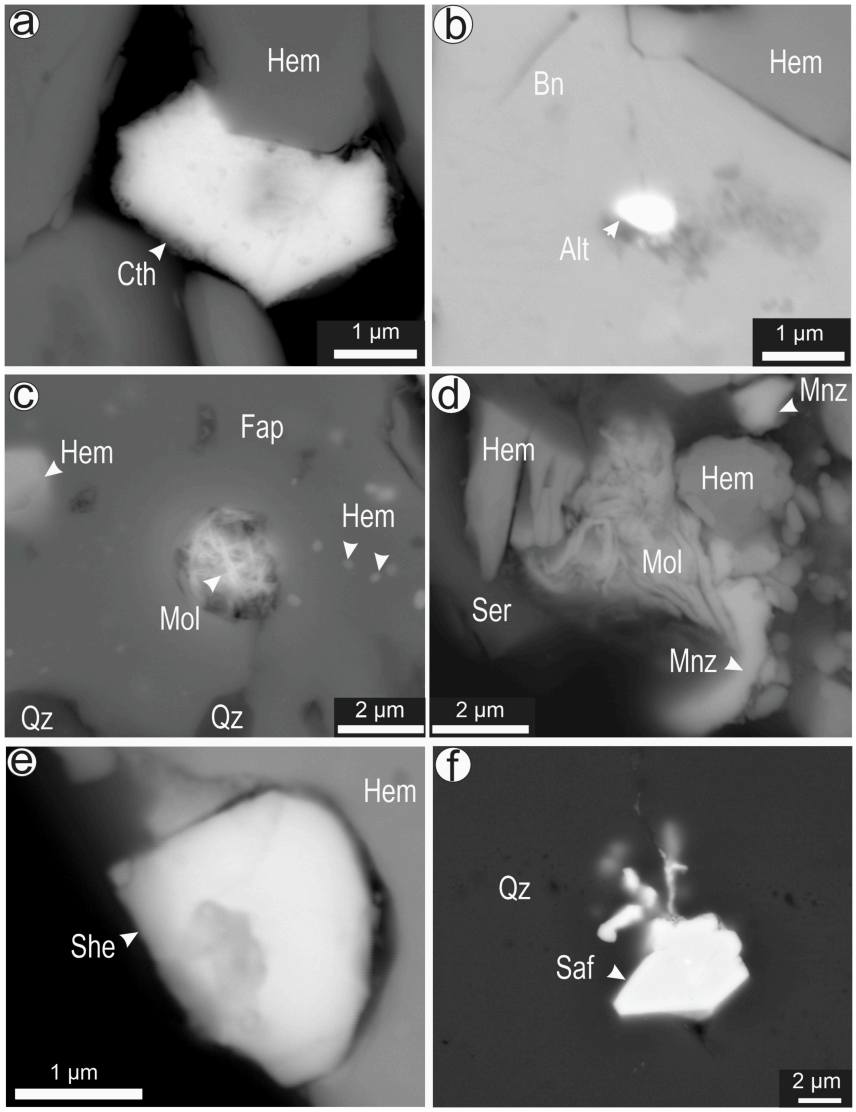



**Figure 13.** BSE images showing the occurrence of trace ore minerals. (**a**) Clausthalite (Cth) micro-grain enclosed within hematite (Hem). (**b**) Inclusion of altaite (Alt) in bornite (Bn). (**c**) Molybdenite (Mol) hosted within gangue minerals. Fap—fluorapatite. (**d**) Molybdenite in association with monazite (Mnz) and gangue minerals. Ser—sericite. (**e**) Inclusion of scheelite (She) within hematite. (**f**) Safflorite (Saf) enclosed within quartz (Qz).

#### 4.8.3. Gangue Mineralogy

Hematite and quartz are the most abundant gangue minerals. MLA data indicates that quartz is more abundant in the three coarsest fractions, whereas hematite dominates the finer fractions. This difference is reflected in the textural associations of the two minerals: hematite commonly occurs with quartz, but also with other gangue minerals such as sericite, chlorite, baryte ($BaSO_4$), and Fe–Ti oxides. Hematite is also intergrown with carbonates, notably siderite and/or dolomite, indicative of the diverse ore types at Prominent Hill. Hematite frequently hosts small mineral inclusions or occurs in close association with a range of REE minerals, dominantly monazite and florencite, but also bastnäsite and synchysite (Figures 6d–h and 7a–c), alongside uraninite and other U (Figures 9 and 10e,f) as well as sub-micron-scale inclusions of scheelite. Quartz, in contrast, is typically observed with other silicates, especially sericite, or chlorite, which are often intergrown (Figure 12g). Quartz is observed to host U-minerals and REE minerals (Figure 8i,j).

Ilmenite ($FeTiO_3$) and rutile, the principal Ti-bearing minerals, are both common, particularly in the coarser fractions, where they commonly occur alongside hematite and

various gangue minerals. Ilmenite displays disparate textures and a strong association with pyroxene and feldspar hinting at an origin from the mafic host lithologies (basaltic andesite in the mineralization footwall [31]). A polymineralic particle in the +125 µm fraction is composed of intergrown hematite–ilmenite, compositionally zoned augite, $(Ca,Mg,Fe)_2Si_2O_6$, and labradorite, $(Ca,Na)(Si,Al)_4O_8$ (Figure 14a,b). Fluorapatite is observed in association with ilmenite and pyroxene. Networks of fine lamellar intergrowths between hematite and ilmenite are observed in association with labradorite, oligoclase and ferro-augite (Figure 14c). In other cases, homogeneous, sub-euhedral ilmenite forms cores of areas comprising hematite and hematite mottled with tiny ilmenite inclusions (Figure 14d).

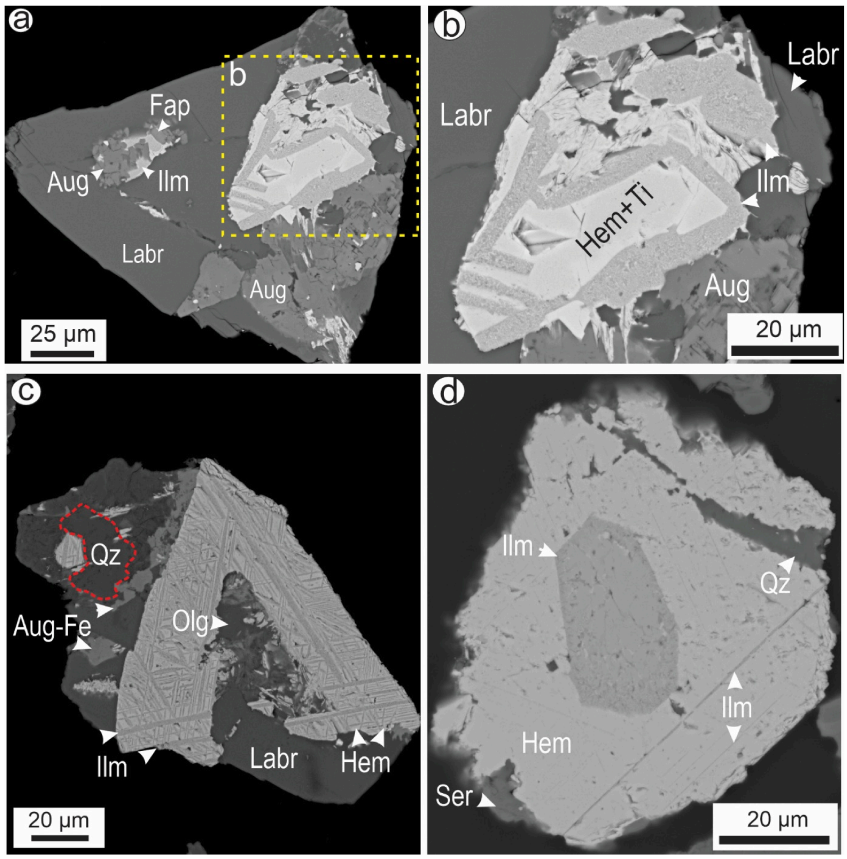



**Figure 14.** BSE images illustrating textural aspects of ilmenite. (**a**) Polymineralic particle shows possible replacement of ilmenite (Ilm) by hematite (Hem) enclosed within augite (Aug) and labradorite (Labr). (**b**) Detail from (**a**) showing ilmenite–hematite replacement. (**c**) Trellis ilmenite exsolved in igneous hematite associated with labradorite. Note small anhedral grains of ferro-augite (Aug-Fe). Dashed red line indicates mineral boundaries otherwise not easily distinguishable. (**d**) Sub-circular ilmenite zone within hematite. Olg—oligoclase; Fap—fluorapatite; Qz—quartz; Ser—sericite.

Rutile is often present as micro-veins that exhibit incomplete replacement by hematite and are enclosed within phases such as sericite (Figure 15a) or are associated with sericite and quartz (Figure 15b). In addition, rutile frequently forms crystallographically oriented lamellae in hematite (Figure 15c), and in some cases, parallel sets of rutile lamellae are hosted within hematite and associated with dolomite (Figure 15d). Some intriguing textures involving rutile or ilmenite are observed, witnessing to both the diversity of host rocks present in the deposit and the complexity of metasomatic reactions during ore formation. These include hematite–rutile symplectites (Figure 15e) enclosed within an intergrowth of sericite and chlorite. EDS analysis of rutile within this symplectite shows 16.6 wt.% Zr, suggesting that this may be a sub-micrometre-scale intergrowth with baddelyite ($ZrO_2$) or possibly srilankite ($ZrTi_2O_6$).

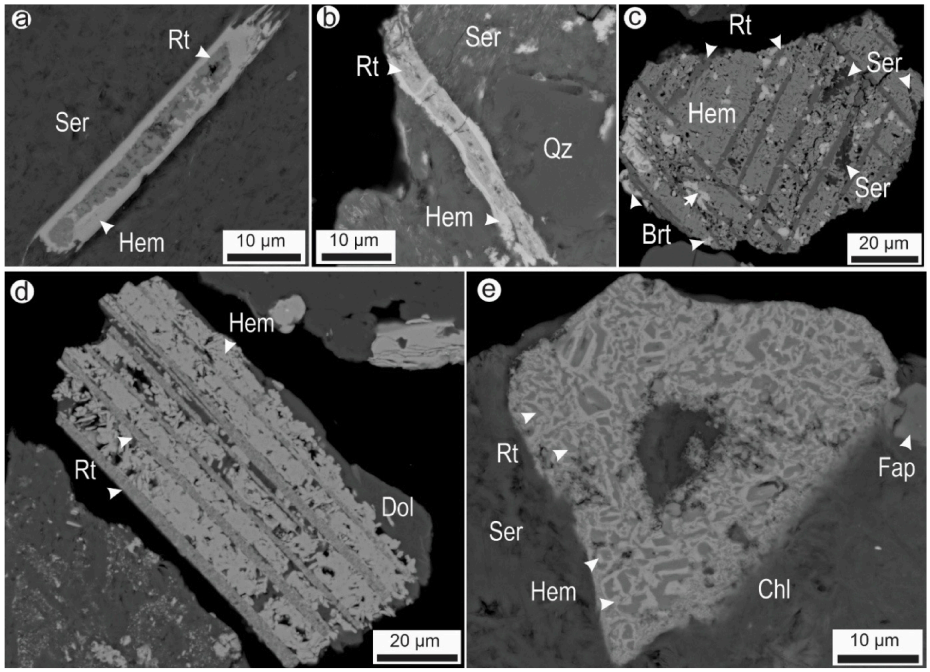



**Figure 15.** BSE images showing aspects of rutile (Rt). (**a**,**b**) Rutile micro-veinlet enclosed within sericite (Ser) and quartz (Qz). (**c**) Polymineralic particle showing rutile micro-vein within hematite (Hem) and association with sericite and baryte (Brt). (**d**) Parallel bands of rutile and hematite associated with dolomite (Dol). (**e**) Symplectite-like intergrowth of rutile and hematite within intergrowth of sericite and chlorite (Chl). Fap—fluorapatite.

## 5. Discussion

### *5.1. Chondrite-Normalized REE Fractionation and Metasomatism*

REE-bearing species in the tailings are dominated by minerals that preferentially incorporate LREE on crystal-chemical grounds; discrete HREE-dominant phases are minor or absent, effectively mirroring the bulk composition of the tailings and the hydrothermal fluid(s) from which they precipitated. As such, the chondrite-normalized fractionation patterns provide only limited insight into evolutionary processes (e.g., [45]). HREE-hosting minerals like xenotime or apatite exhibit more diverse and process-sensitive REE signatures, owing to differences in site size, substitution mechanisms and redox sensitivity, making them more informative recorders of magmatic and hydrothermal evolution [46–48].

Chondrite-normalized REE fractionation patterns (Figure 2a) show a clear positive Eu anomaly, accompanied by subtle negative Sm and Gd anomalies. Positive Eu anomalies are generated in reducing environments in which $Eu^{2+}$, with a smaller ionic radius (1.14 Å), prevails over $Eu^{3+}$ (1.39 Å; [49]). Eu reduction processes are generated in high-temperature conditions [50]. Ores precipitated from hydrothermal solutions are often characterized by strong LREE enrichment and a positive Eu anomaly. With increasing temperature, Ce, Gd, and Y anomalies, if present, are eliminated through ion exchange with other minerals, while Eu anomalies persist [51].

$Eu^{2+}$ is preferentially incorporated into plagioclase, where it substitutes for $Ca^{2+}$ [52,53]. Both MLA data and SEM observations confirm the scarcity of plagioclase (1.16 wt.%), hinting at replacement and near-complete obliteration of the feldspar, which was plausibly a major component of the volcanic host rocks prior to Fe-metasomatism. Despite the rarity of plagioclase, a pronounced positive anomaly is nevertheless preserved in the REE minerals.

During the intense metasomatism following the onset of IOCG systems, igneous feldspars record progressive transformation of igneous feldspar to hydrothermal phases. This is accompanied by redistribution of trace elements, including REEs. At Olympic Dam,

Kontonikas-Charos et al. [54,55] demonstrated that hydrothermal albitization and feldspar replacement reactions involve coupled dissolution–reprecipitation (CDR) processes that release REEs previously incorporated in feldspars into the local fluid environment, thereby facilitating the formation of discrete REE-bearing minerals. Relict feldspars in host rocks located proximal to ore feature highly modified REE signatures that reflect removal of REEs from the feldspar lattice [55]. Metasomatic fluid–rock interaction thus not only alters primary phases, plagioclase in this case, but is also a powerful driver of REE-phosphate and -fluorocarbonate compositions in IOCG deposits and flotation tailings. Nanoscale evidence of pseudomorphic replacement of feldspars by REE fluorocarbonates [56] underscores the role of feldspar breakdown in supplying key elements (e.g., Ca, P, and LREEs) into fluids that ultimately precipitate discrete REE minerals.

Overall, these results show that REE enrichment in the tailings is not just a simple concentration effect but rather reflects, in part, initial fluid–rock reaction that is evidenced both structurally and chemically in both the primary minerals, where preserved, and new-formed minerals. This is, however, not the end of the story, as will be shown below. Prominent Hill and its kin deposits in the Olympic Cu-Au Province show ample evidence of superimposed cycles of fluid-driven remobilization and reprecipitation of elements which further modify and refine the distribution patterns generated by early metasomatism. Importantly, much of the latter modification does not require an input of fluids nor elements from external sources, but rather a closed-system recycling of materials already present.

### *5.2. Size Dependency of REE Distributions*

Most REE minerals show higher proportions of liberation within the fine size fractions, suggesting that there is theoretical potential for recovery. However, despite the high degree of liberation, recovery of REE minerals from these fine fractions will be challenging due to their small particle size, which negatively affects separation efficiency during physical beneficiation. Factors such as poor particle settling, increased entrainment, and reduced separation selectivity during flotation or gravity concentration can significantly hinder effective recovery, underscoring the trade-off between enhanced mineral liberation and diminished process efficiency in fine-grained fractions.

For instance, fine and ultra-fine mineral particles (<40–50 μm) are known to exhibit poor flotation performance because low particle mass and high surface energy reduce bubble–particle collision and attachment efficiency, while increasing reagent consumption and entrainment of gangue minerals into the concentrate [6,56]. Additionally, gravity and magnetic separation efficiency declines sharply with decreasing particle size as hydrodynamic drag forces dominate over selective forces, misplacing valuable minerals into the tailings [6].

In addition, REE minerals are commonly spatially associated with discrete U-bearing phases. According to the MLA data, coffinite shows association with monazite within the fine fractions, +C3, +C4 and +C5, with percentages of association of 2.58, 2.31, and 5.79%, respectively. Monazite and REE fluorocarbonates are also capable of structurally incorporating U and Th into their crystal lattices through ionic substitution (e.g., [57]), even if relevant data for these minerals (in material from Olympic Dam) shows only modest concentrations [58,59]. Consequently, beneficiation processes aimed at upgrading REE mineral fractions tend to simultaneously concentrate U and Th, yielding an REE concentrate that may be sufficiently radioactive, thus potentially negatively impacting transport and/or marketing of the concentrate. Furthermore, the presence of U, Th, and their daughter radionuclides introduce substantial downstream complications, including stricter regulatory oversight, limitations on storage and transport, enhanced worker protection requirements, and more complex permitting pathways [60]. Additional, often costly, processing steps

are often required to remove or manage U and Th prior to refining, increasing technical complexity, operational costs, and environmental management obligations [61].

### *5.3. Monazite Replacement: Phosphates and Fluorocarbonates*

Monazite is the principal REE-bearing mineral identified in the studied samples. In other deposits, monazite is reported to be replaced by various minerals, notably phosphates such as apatite and allanite [62]. Monazite is partially replaced by florencite in tailings from Carrapateena [15]. We see no evidence for replacement of monazite by apatite, and allanite is absent altogether. In contrast, monazite is a relatively scarce REE mineral at Olympic Dam and is not observed to coexist with florencite [59].

In the present study, monazite is replaced by synchysite (Figure 6j) and, conspicuously, never by bastnäsite. Prior work elsewhere has established that both monazite and allanite are commonly replaced by rhabdophane via CDR reactions [63,64], but are also reported to be replaced by hydrous REE carbonates "like hydroxylbastnaesite-(Ce) or synchysite" [62], particularly when $CO_2$-rich fluids are present.

Conversely, monazite can directly replace bastnäsite at 220 °C during hydrothermal alteration in acidic and phosphate-rich environments [65]. According to Schulz [62], the irregular shapes of small monazite grains found within aggregates of other phosphates like allanite are not relics preserved following incomplete replacement but instead are newly crystallized monazite. This distinction is important because it highlights that grains which have the appearance of surviving relicts of primary minerals may instead record subsequent crystallization events, reflecting the dynamic nature of fluid–rock interaction and the mobility of REEs and probably also phosphorus during superimposed alteration. Such textures therefore cannot be assumed to represent simple preservation of an early paragenesis but may instead result from dissolution–reprecipitation processes that overprint the original assemblage. In this context, mineral chemistry and microstructural relationships become critical for distinguishing true relic phases from secondary growth. The apparent textural continuity may thus mask significant chemical re-equilibration, emphasizing that element redistribution during hydrothermal alteration can be more extensive than is evident from petrographic observations alone.

### *5.4. REE Fluorocarbonates: Intergrowth and Replacement Relationships*

Members of the bastnäsite–synchysite series commonly form intimately intergrown domains that reflect the modular structures of these species. Such intergrowths are reported from carbonatite-related REE deposits [66,67] but are also known from IOCG deposits of the Olympic Cu-Au Province [68,69]. Fluorocarbonates are especially abundant at Olympic Dam, where they are the dominant REE minerals [27,57].

Intergrowths of bastnäsite and synchysite, which often extend to the nanoscale, likely reflect small fluctuations in Ca activity, $CO_3^{2-}$, $F^-$ and temperature in the mineralizing fluid. Small shifts in phase stability promote the partial replacement of bastnäsite by Ca-rich members, notably synchysite and parisite, during cooling or fluid evolution [70]. High-resolution imaging of nanoscale intergrowths of bastnäsite and synchysite modules in REE fluorocarbonates [69] reflects a gradual progression toward chemical equilibrium. These fine-scale domains record stepwise compositional changes between end-member phases, highlighting the influence of evolving physicochemical conditions during metasomatism and accompanying mineralization.

Fluorocarbonates are, however, not always the most common REE minerals in IOCG deposits of the Olympic Cu-Au Province. In both Prominent Hill and Carrapateena [15], REEs are largely hosted by phosphates, monazite and florencite. Ongoing work by the authors at the recently discovered Oak Dam prospect shows the presence of distinct domains

in which bastnäsite, monazite (±xenotime) and florencite are the dominant REE hosts. These differences, both between and within deposits, highlight distinct mineralization styles across the province but also variations in local geochemical environments during primary mineralization, and during subsequent episodes of remobilization–recrystallization. Parameters that impact REE mineralogy include fluid composition, temperature, pH, and the availability of phosphate versus carbonate in the system [71]. Structural controls, such as faulting and fracture networks, may also influence fluid pathways and element mobility, leading to preferential precipitation of specific REE minerals in different deposits or parts thereof [72]. Such variations highlight the distinct mineralization styles of individual deposits and carry implications for the longer-term viability of REE exploitation.

The bastnäsite reported here frequently occurs intergrown with synchysite and parisite (Figure 8h–j), forming composite grains that might be interpreted as recording a progressive evolution of REE-fluorocarbonate mineralization as described elsewhere. On closer inspection, these textures exceed those of a simple intergrowth and more likely reflect a systematic yet incomplete replacement of bastnäsite by synchysite or parisite. Bastnäsite is only preserved within zones of intense alteration and fractures (Figure 8a,b) and as relicts preserved at the late stage of replacement (Figure 8j) within parisite. Constraints on the timing of this replacement are impossible to make, yet the conspicuous morphology of some synchysite could indicate formation under extensional conditions.

The present study has identified significant compositional differences between primary and replacive REE carbonate phases, notably the systematically lower F content of synchysite compared to coexisting bastnäsite. If interpreted in terms of OH-for-F substitution and assuming full Z-site occupancy, this could suggest that the replacive Ca-rich phases contain greater OH, thus mirroring the scenario outlined by Ondrejka et al. [63] and similar OH–F exchange mechanisms reported for apatite-group and REE-bearing minerals in fluid-mediated alteration systems [73,74]. Verification through in situ OH analysis would be needed to confirm this, but the trend provides a useful chemical marker for relative timing of REE mineralization.

### *5.5. Uranium Mobility and Replacement Relationships*

The new data from Prominent Hill bolster the recognition that uranium carbonates occur intergrown with uraninite within multiple IOCG systems across the Olympic Cu-Au Province. Examples include Carrapateena [15] and comparable associations in both Olympic Dam and Oak Dam (authors' unpublished data). Textural relationships suggest that wyartite formed during a late-stage hydrothermal overprint, partially replacing uraninite.

Coupled dissolution–reprecipitation [75] is a fundamental reaction mechanism observed in multiple mineral groups at Olympic Dam (e.g., [43,47,54,55,76–79]) and has clearly played a major role in shaping the mineralogy and texture of ores as observed today. In a CDR process, a fluid undersaturated with respect to a primary mineral initiate its dissolution, forming a thin interfacial boundary layer at the mineral–fluid interface [75,80]. As dissolution proceeds, the local boundary layer can become supersaturated with respect to a more stable secondary phase, allowing simultaneous replacement that preserves the original mineral shape while altering its internal composition and structure [81].

Wyartite is a secondary uranium mineral formed in an oxidizing carbonate-rich environment [82]. Alongside essential Ca, minor amounts of Fe, Mg, and Mn are noted in EDS data. We assume that these elements were incorporated into wyartite during alteration of uraninite and relate their presence to dissolution of diverse carbonate minerals (calcite, dolomite, siderite, rhodochrosite, etc.) from the host lithologies.

The compositional and textural diversity of U-(carbonate) minerals suggest apparent progressive replacement pathways, such as the transformation of uraninite into Cu–Fe sulphides, notably chalcopyrite (Figure 10a) and bornite (Figure 10d), previously constrained at Olympic Dam by Macmillan et al. [77]. Uraninite can be replaced by wyartite and other uranyl carbonates [83], as seen in Figure 10a–c, or by silicates like coffinite (Figure 10e–h). The actual processes involved are, however, more complex than a simple single-stage replacement reaction. Each transformation is influenced by a combination of factors, including fluid composition, temperature, redox conditions, and the presence of catalytic ions such as $Ca^{2+}$ and $Mg^{2+}$, which significantly affect uranyl carbonate speciation and mobility in solution [84], and potentially also their stability. Variations in these parameters during fluid evolution can promote different mineral assemblages, allowing uraninite to be replaced by sulphides, silicates, or uranyl carbonates depending on the prevailing chemical environment [85]. Furthermore, fluid–rock interaction and local chemical gradients can produce microscale heterogeneity, leading to spatially variable alteration textures within a single grain or domain [85]. Additionally, these pathways may not occur uniformly; multiple alteration reactions can happen simultaneously or in overlapping stages, and intermediate phases might form transiently before stabilizing as the observed mineral assemblages. Therefore, while the observed compositional trends provide valuable clues, the real mineralogical evolution reflects a dynamic interplay of physicochemical conditions rather than a single, straightforward pathway. These compositional variations indicate progressive replacement pathways from uraninite → Cu–Fe sulphides (bornite or chalcopyrite) and from uraninite → wyartite or coffinite.

Coffinite is a secondary uranium mineral, widely formed via a process of dissolution of pre-existing uraninite [86–89]. Uranium released from uraninite may exhibit limited mobility and recrystallize as coffinite in the near vicinity [89], as illustrated here (Figure 10e–h). Conversion from uraninite to coffinite is marked by an increase in Si and Y coupled with a marked decrease in Pb content. Released Pb may not migrate long distances and will form secondary galena, thus explaining the fine inclusions of galena close to uraninite relicts (Figure 10h). Some mobilized uranium may, however, be transported over much longer distances, even hundreds of metres, ultimately crystallizing as the ubiquitous fine-grained clausthalite and altaite found in these ores [44]. The conspicuous Pb-isotope signatures of these phases [90] support remobilization and fixation as Pb-chalcogenides during a superimposed event that took place some hundreds of millions of years after initial formation. This scenario is fully consistent with the different textural varieties of uranium minerals, their disparate Pb contents [43,88,91], and the observed multiple populations of uraninite ages [92].

The presence of several distinct textures involving uraninite indicates a complex and multi-stage history of uranium mineralization at Prominent Hill, comparable to that recognized across the region. These findings and interpretations could be assessed by geochronological studies of U-bearing minerals from the Prominent Hill deposit.

Uraninite is not simply preserved as relicts of an early generation partially replaced by coffinite and/or wyartite. Instead, it occurs in several distinct textural forms, such as near-perfect cubic crystals with variable Pb content, small inclusions within hematite and other minerals, and also replacing a range of different mineral species.

Cubic uraninite likely represents primary crystallization under stable (near)-equilibrium conditions favourable for nucleation and steady growth. In contrast, the disparate replacement textures suggest later fluid-mediated alteration, in which earlier minerals were partially dissolved and uraninite reprecipitated in their place. Uraninite inclusions within other phases indicate additional stages of growth, either during early mineral formation or during later overprinting events. Together, these different textures point to multiple episodes of uranium

mobilization, dissolution, and reprecipitation, reflecting a dynamic and evolving mineralizing system rather than a single, preserved generation of uraninite.

The relationships between REEs and U further support this interpretation. Both rare earth elements and uranium can be readily remobilized, particularly in oxidizing, fluid-rich environments. Over geological time, changes in redox state, temperature, fluid composition, and deformation can repeatedly remobilize uranium. This can lead to a decoupling or re-association of REEs and U during different stages, recording a long history of metasomatism, fluid interaction, and mineral re-equilibration within the system.

## 6. Conclusions and Implications

IOCG tailings represent a substantial and underexplored repository of REEs that could complement the primary commodities copper, gold, and silver. Systematic mineralogical and geochemical investigation of fresh tailings provides a foundation for assessing element distribution, retention, recovery potential, and long-term geochemical behaviour under oxidative conditions in tailings storage facilities.

This study demonstrates the complexity of REE mineral assemblages at the micron scale and highlights the significance of replacement relationships among REE phosphates and fluorocarbonates. These textures are consistent with REE remobilization and reprecipitation during prolonged geological evolution. A close association between U and REEs was also identified, with important implications for the production of clean REE concentrates. Uranium mineralization is characterized by replacement processes, including the alteration of uraninite to coffinite and secondary U-carbonates.

The mineralogical record preserved in the tailings provides insight into the processes governing trace-element incorporation, retention, and redistribution during ore formation, hydrothermal overprinting, and subsequent alteration. The occurrence and associations of REE- and U-bearing phases with iron oxides, gangue minerals, sulphides, and other hosts reflect the evolution of hydrothermal fluids and the physicochemical conditions controlling element partitioning. These observations contribute to improved geological models for REE and U enrichment in IOCG systems.

This work also contributes to broader efforts to evaluate the resource potential of tailings across the Olympic Cu–Au Province [93]. The results identify opportunities for resource recovery that complement ongoing efforts to produce REE concentrates from IOCG ores [6,94]. Future studies will integrate mineralogical data from Prominent Hill tailings and flotation concentrates to evaluate differences in REE- and U-bearing mineral assemblages, their associations with Cu-(Fe) sulphides, and the distribution of trace elements with potential by-product value between copper concentrates and tailings.

Overall, the results highlight the potential of IOCG systems as sources of both primary commodities and critical minerals. Detailed mineralogical characterization is essential for evaluating resource recovery opportunities, improving resource utilization, supporting sustainable mining practices, and informing long-term management of mineral resources.

**Supplementary Materials:** The following supporting information can be downloaded at: https://www.mdpi.com/article/10.3390/min16070671/s1, Table S1. List of minerals identified in the Prominent Hill tailings. Figure S1. Bar charts showing associations of the five main REE minerals in three coarse size fractions. Figure S2. Bar charts showing associations of the five main REE minerals in three medium-size fractions.

**Author Contributions:** N.J.C. and K.E. designed the research. K.E. and C.L.C. provided advice and guidance throughout. All presented microanalytical data was acquired by Z.H. The manuscript was written by Z.H. and N.J.C., with contributions from K.E. and C.L.C. All authors have read and agreed to the published version of the manuscript.

**Funding:** This work was funded by Australian Research Council Grants LP200100156 (Critical Metals from Complex Copper Ores) and LP240200662 (Lanthanides and actinides in copper ores, a pas de deux in geological time), co-supported by BHP Copper South Australia.

**Data Availability Statement:** Full datasets (including raw analytical data, MLA statistical results, and image materials) are either included within this article and its Supplementary Materials, or available from the authors upon request and at the discretion of the funding industry partner.

**Acknowledgments:** We gratefully acknowledge the assistance with microanalysis provided by staff at Adelaide Microscopy. The authors acknowledge the constructive comments of three anonymous reviewers which helped us refine the ideas expressed in this article.

**Conflicts of Interest:** Kathy Ehrig is an employee of BHP Copper South Australia. The paper reflects the views of the scientists and not the company.

## References

1. Williams, P.J.; Barton, M.D.; Johnson, D.A.; Fontbote, L.; de Haller, A.; Mark, G.; Oliver, N.H.S.; Marschik, R. Iron oxide copper-gold deposits: Geology, spacetime distributions, and possible modes of origin. *Econ. Geol.* **2005**, *100*, 371–405. [CrossRef]
2. Smith, M.P.; Moore, K.; Kavecsánszki, D.; Finch, A.A.; Kynický, J.; Wall, F. From mantle to critical zone: A review of large and giant rare earth element deposits. *Geosci. Front.* **2016**, *7*, 315–334. [CrossRef]
3. Skirrow, R.G. Iron oxide copper-gold (IOCG) deposits—A review (part 1): Settings, mineralogy, ore geochemistry and classification. *Ore Geol. Rev.* **2022**, *140*, 104569. [CrossRef]
4. Dushyantha, N.; Batapola, N.; Ilankoon, I.M.S.K.; Rohitha, S.; Premasiri, R.; Abeysinghe, B.; Ratnayake, N.; Dissanayake, K. The story of rare earth elements (REEs): Occurrences, global distribution, genesis, geology, mineralogy and global production. *Ore Geol. Rev.* **2020**, *122*, 103521. [CrossRef]
5. Balaram, V. Geoscience Frontiers Rare earth elements: A review of applications, occurrence, exploration, analysis, recycling, and environmental impact. *Geosci. Front.* **2019**, *10*, 1285–1303. [CrossRef]
6. Abaka-Wood, G.B.; Addai-Mensah, J.; Ehrig, K.; Skinner, W. Recovery of rare earth element minerals from iron oxide–silicate rich tailings: A review. *Minerals* **2022**, *12*, 259.
7. Whitworth, A.J.; Forbes, E.; Verster, I.; Jokovic, V.; Awatey, B.; Parbhakar-Fox, A. Review on advances in mineral processing technologies suitable for critical metal recovery from mining and processing wastes. *Clean. Eng. Technol.* **2022**, *7*, 100451. [CrossRef]
8. Abbadi, A.; Mucsi, G. A review on complex utilization of mine tailings: Recovery of rare earth elements and residue valorization. *J. Environ. Chem. Eng.* **2024**, *12*, 113118. [CrossRef]
9. Kursunoglu, S. A review on the recovery of critical metals from mine and mineral processing tailings: Recent advances. *J. Sustain. Metall.* **2025**, *11*, 2023–2050. [CrossRef]
10. Jamieson, H.E. Geochemistry and Mineralogy of Solid Mine Waste: Essential Knowledge for Predicting Environmental Impact. *Elements* **2011**, *7*, 381–386. [CrossRef]
11. Jamieson, H.E.; Walker, S.R.; Parsons, M.B. Mineralogical characterisation of mine waste. *Appl. Geochem.* **2015**, *57*, 85–105. [CrossRef]
12. Zhao, T.-Y.; Li, W.-L.; Kelebek, S.; Choi, Y.; Wu, C.-Q.; Zhang, W.-J.; Wang, C.-Y.; Zhao, Z.-W.; Sadri, F. A comprehensive review on rare earth elements: Resources, technologies, applications, and prospects. *Rare Met.* **2025**, *44*, 7011–7040. [CrossRef]
13. Hajdu-Rahkama, R.; Kinnunen, P. Tailings Valuation: Opportunities to secure rare earth supply and make mining environmentally more sustainable. *J. Clean. Prod.* **2025**, *520*, 146147. [CrossRef]
14. International Energy Agency. Critical Minerals Market Review: Key Market Trends. 2023. Available online: https://www.iea.org/reports/critical-minerals-market-review-2023/key-market-trends (accessed on 22 May 2025).
15. Habibi, Z.; Cook, N.J.; Ehrig, K.; Ciobanu, C.L.; Campo-Rodriguez, Y.T.; King, S.A. Minor and Trace Elements in Copper Tailings: A Mineralogical and Geometallurgical Approach to Identify and Evaluate New Opportunities. *Minerals* **2025**, *15*, 1018. [CrossRef]
16. Guanira, K.; Valente, T.M.; Ríos, C.A.; Castellanos, O.M.; Salazar, L.; Lattanzi, D.; Jaime, P. Methodological approach for mineralogical characterization of tailings from a Cu(Au,Ag) skarn type deposit using QEMSCAN (Quantitative Evaluation of Minerals by Scanning Electron Microscopy). *J. Geochem. Explor.* **2020**, *209*, 106439. [CrossRef]
17. Peelman, S.; Kooijman, D.; Sietsma, J.; Yang, Y. Hydrometallurgical recovery of rare earth elements from mine tailings and WEEE. *J. Sustain. Metall.* **2018**, *4*, 367–377. [CrossRef]
18. Ba, N.B.; Souissi, R.; Manai, F.; Taviche, I.K.; Bejaoui, B.; Bagga, M.A.; Souissi, F. Mineralurgical and Environmental Characterization of the Mine Tailings of the IOCG Mine of Guelb Moghrein, Akjoujt, Mauritania. *Appl. Sci.* **2024**, *14*, 1591. [CrossRef]

19. Velten, R.Z.; Scheuermann Filho, H.C.; Rodrigues da Costa, J.P.; Lima, C.A.; Wang, Y.; Coop, M.R.; Consoli, N.C. Geomechanical behaviour of fine- and coarse-grained copper tailings from Brazilian IOCG deposits. *Can. Geotech. J.* **2025**, *62*, 1–21. [CrossRef]
20. Araya, N.; Kraslawski, A.; Cisternas, L.A. Towards mine tailings valorization: Recovery of critical materials from Chilean mine tailings. *J. Clean. Prod.* **2020**, *263*, 121555. [CrossRef]
21. Rollog, M.; Cook, N.J.; Guagliardo, P.; Ehrig, K.J.; Kilburn, M. Radionuclide-bearing minerals in Olympic Dam copper concentrates. *Hydrometallurgy* **2019**, *190*, 105153. [CrossRef]
22. Rollog, M.; Cook, N.J.; Guagliardo, P.; Ehrig, K.; Kilburn, M. Radionuclide distributions in Olympic Dam copper concentrates: The significance of minor hosts, incorporation mechanisms, and the role of mineral surfaces. *Miner. Eng.* **2020**, *148*, 106176. [CrossRef]
23. Ram, R.; Owen, N.D.; Kalnins, C.; Cook, N.J.; Ehrig, K.; Etschmann, B.; Rollog, M.; Fu, W.; Vaughan, J.; Pring, A.; et al. Understanding the mobility and retention of uranium and its daughter products. *J. Hazard. Mater.* **2021**, *410*, 124553. [CrossRef] [PubMed]
24. Reid, A. The Olympic Cu-Au Province, Gawler Craton: A Review of the Lithospheric Architecture, Geodynamic Setting, Alteration Systems, Cover Successions and Prospectivity. *Minerals* **2019**, *9*, 371. [CrossRef]
25. BHP. Annual Report. 2025. Available online: https://www.bhp.com/-/media/documents/investors/annual-reports/2025/250819_bhpannualreport2025.pdf (accessed on 31 July 2025).
26. Ferris, G.M.; Schwarz, M.P.; Heithersay, P. The geological framework, distribution and controls of Fe-oxide Cu-Au mineralisation in the Gawler Craton, South Australia: Part 1: Geological and tectonic framework. In *Hydrothermal Iron Oxide Copper-Gold and Related Deposits: A Global Perspective*; Porter, T.M., Ed.; Porter GeoConsultancy Publishing: Adelaide, Australia, 2002; Volume 2, pp. 9–31.
27. Ehrig, K.; McPhie, J.; Kamenetsky, V. Geology and mineralogical zonation of the Olympic Dam iron oxide Cu-U-Au-Ag deposit, South Australia. *Soc. Econ. Geol. Spec. Publ.* **2012**, *16*, 237–267. [CrossRef]
28. Dmitrijeva, M.; Ehrig, K.J.; Ciobanu, C.L.; Cook, N.J.; Verdugo-Ihl, M.R.; Metcalfe, A.V. Defining IOCG signatures through compositional data analysis: A case study of lithogeochemical zoning from the Olympic Dam deposit, South Australia. *Ore Geol. Rev.* **2019**, *105*, 86–101. [CrossRef]
29. Courtney-Davies, L.; Ciobanu, C.L.; Verdugo-Ihl, M.R.; Cook, N.J.; Slattery, A.; Dmitrijeva, M.; Keyser, W.; Wade, B.P.; Domnick, U.I.; Ehrig, K.; et al. Zircon at the nanoscale records metasomatic processes leading to large magmatic–hydrothermal ore systems. *Minerals* **2019**, *9*, 364. [CrossRef]
30. Belperio, A.; Flint, R.; Freeman, H. Prominent Hill: A hematite-dominated iron oxide copper–gold system. *Econ. Geol.* **2007**, *102*, 1499–1510. [CrossRef]
31. Freeman, H.; Tomkinson, M. Geological setting of iron oxide related mineralisation in the southern Mount Woods Domain, South Australia. In *Hydrothernal Iron Oxide Copper-Gold & Related Depoits: A Global Perspective*; Porter, T.M., Ed.; Advances in the Understanding of IOCG Deposits; PGC Publishing: Adelaide, Australia, 2010; Volume 3, pp. 1–19.
32. Bowden, B.; Fraser, G.; Davidson, G.J.; Meffre, S.; Skirrow, R.; Bull, S.; Thompson, J. Age constraints on the hydrothermal history of the Prominent Hill iron oxide copper-gold deposit, South Australia. *Miner. Depos.* **2017**, *52*, 863–881.
33. Schlegel, T.U.; Heinrich, C.A. Lithology and Hydrothermal Alteration Control the Distribution of Copper Grade in the Prominent Hill Iron Oxide-Copper-Gold Deposit (Gawler Craton, South Australia). *Econ. Geol.* **2015**, *110*, 1953–1994. [CrossRef]
34. Schlegel, T.U.; Wagner, T.; Walle, M.; Heinrich, C.A. Hematite Breccia-Hosted Iron Oxide Copper-Gold Deposits Require Magmatic Fluid Components Exposed to Atmospheric Oxidation: Evidence from Prominent Hill, Gawler Craton, South Australia. *Econ. Geol.* **2018**, *113*, 597–644. [CrossRef]
35. Carter, D.; Belperio, T.; Freeman, H. The discovery of the Prominent Hill copper-gold deposit, South Australia. In *Proceedings of the NewGenGold 2003 Conference, Case Histories of Discovery, Perth, Australia, November 2003*; Louthean Media: Perth, Australia, 2003; pp. 102–116.
36. BHP. Prominent Hill—BHP. 2025. Available online: https://www.bhp.com/what-we-do/global-locations/australia/south-australia/prominent-hill (accessed on 30 January 2026).
37. Cooke, H.M. *Anthropogenic Mineral Systems: Material Flow, Geochemistry, and Mineralogy of the Prominent Hill Tailings Deposit*; School of Physical Sciences, The University of Adelaide: Adelaide, Australia, 2023. Available online: https://hdl.handle.net/2440/146283 (accessed on 28 May 2026).
38. Alfonso, P. Editorial for Special Issue "Mineral Liberation". *Minerals* **2021**, *11*, 47. [CrossRef]
39. ALS Global. *Quantitative Mineralogical Services*; ALS Limited: Brisbane, Australia, 2022; 8p. Available online: https://www.alsglobal.com/en/ (accessed on 7 September 2025).
40. McDonough, W.F.; Sun, S.S. The composition of the Earth. *Chem. Geol.* **1995**, *120*, 223–253. [CrossRef]
41. Hughes, J.M.; Rakovan, J.F. Structurally Robust, Chemically Diverse: Apatite and Apatite Supergroup Minerals. *Elements* **2015**, *11*, 165–170. [CrossRef]

42. Verdugo-Ihl, M.R.; Ciobanu, C.L.; Cook, N.J.; Ehrig, K.J.; Courtney-Davies, L.; Gilbert, S. Textures and U-W-Sn-Mo signatures in hematite from the Olympic Dam Cu-U-Au-Ag deposit, South Australia: Defining the archetype for IOCG deposits. *Ore Geol. Rev.* **2017**, *91*, 173–195. [CrossRef]
43. Macmillan, E.; Cook, N.J.; Ehrig, K.; Ciobanu, C.L.; Pring, A. Uraninite from the Olympic Dam IOCG-U-Ag deposit: Linking textural and compositional variation to temporal evolution. *Am. Miner.* **2016**, *101*, 1295–1320. [CrossRef]
44. Owen, N.D.; Ciobanu, C.L.; Cook, N.J.; Slattery, A.; Basak, A. Nanoscale study of clausthalite-bearing symplectites in Cu-Au-(U) ores: Implications for ore genesis. *Minerals* **2018**, *8*, 67. [CrossRef]
45. Migdisov, A.; Guo, X.; Nisbet, H.; Xu, H.; Williams-Jones, A.E. Fractionation of REE, U, and Th in natural ore-forming hydrothermal systems: Thermodynamic modeling. *J. Chem. Thermodyn.* **2019**, *128*, 305–319. [CrossRef]
46. Krneta, S.; Cook, N.J.; Ciobanu, C.L.; Ehrig, K.; Kontonikas-Charos, A. The Wirrda Well and Acropolis prospects, Gawler Craton, South Australia: Insights into evolving fluid conditions through apatite chemistry. *J. Geochem. Explor.* **2017**, *181*, 276–291. [CrossRef]
47. Krneta, S.; Ciobanu, C.L.; Cook, N.J.; Ehrig, K.J. Numerical modeling of REE fractionation patterns in fluorapatite from the Olympic Dam deposit (South Australia). *Minerals* **2018**, *8*, 342. [CrossRef]
48. Hentschel, F.; Janots, E.; Trepmann, C.A.; Magnin, V.; Lanari, P. Corona formation around monazite and xenotime during greenschist-facies metamorphism and deformation. *Eur. J. Miner.* **2020**, *32*, 521–544. [CrossRef]
49. Shannon, R.D. Revised effective ionic radii and systematic studies of interatomic distances in halides and chalcogenites. *Acta Cryst.* **1976**, *A32*, 751–767. [CrossRef]
50. Tepe, N.; Bau, M. Distribution of rare earth elements and other high field strength elements in glacial meltwaters and sediments from the western Greenland ice sheet; evidence for different sources of particles and nanoparticles. *Chem. Geol.* **2015**, *412*, 59–68. [CrossRef]
51. Möller, P.; Dulski, P.; De Lucia, M. REY patterns and their natural anomalies in waters and brines: The correlation of Gd and Y anomalies. *Geosciences* **2021**, *11*, 24. [CrossRef]
52. Weill, D.F.; Drake, M.J. Europium Anomaly in Plagioclase Feldspar: Experimental Results and Semiquantitative Model. *Science.* **1973**, *180*, 1059–1060. [CrossRef] [PubMed]
53. Sager, M.; Wiche, O. Rare earth elements (REE): Origins, dispersion, and environmental implications—A comprehensive review. *Environments* **2024**, *11*, 24. [CrossRef]
54. Kontonikas-Charos, A.; Ciobanu, C.L.; Cook, N.J.; Ehrig, K.; Krneta, S.; Kamenetsky, V.S. Feldspar evolution in the Roxby Downs Granite, host to Fe oxide Cu-Au-(U) mineralisation at Olympic Dam, South Australia. *Ore Geol. Rev.* **2017**, *80*, 838–859. [CrossRef]
55. Kontonikas-Charos, A.; Ciobanu, C.L.; Cook, N.J.; Ehrig, K.; Ismail, R.; Krneta, S.; Basak, A. Feldspar mineralogy and rare-earth element remobilization in iron oxide–copper–gold systems from South Australia: A nanoscale study. *Miner. Mag.* **2018**, *81*, 981–1006. [CrossRef]
56. Farrokhpay, S.; Filippov, L.; Fornasiero, D. Flotation of fine particles: A review. *Miner. Process. Extr. Metall. Rev.* **2021**, *42*, 473–483.
57. Förster, H.J. The chemical composition of REE-Y-Th-U-rich accessory minerals in peraluminous granites of the Erzgebirge-Fichtelgebirge region, Germany. Part II: Xenotime. *Am. Miner.* **1998**, *83*, 1302–1315. [CrossRef]
58. Schmandt, D.S.; Cook, N.J.; Ciobanu, C.L.; Ehrig, K.; Wade, B.P.; Gilbert, S.; Kamenetsky, V.S. Rare earth element fluorocarbonate minerals from the Olympic Dam Cu-U-Au-Ag deposit, South Australia. *Minerals* **2017**, *7*, 202. [CrossRef]
59. Schmandt, D.S.; Cook, N.J.; Ciobanu, C.L.; Ehrig, K.; Wade, B.P.; Gilbert, S.; Kamenetsky, V.S. Rare earth element phosphate minerals from the Olympic Dam Cu–U–Au–Ag deposit, South Australia: Recognizing temporal-spatial controls on REE mineralogy in an evolved IOCG system. *Can. Miner.* **2019**, *57*, 3–24. [CrossRef]
60. International Atomic Energy Agency. *Self-Assessment of Capacity Building for Nuclear, Radiation, Transport and Waste Safety, and Emergency Preparedness and Response*; International Atomic Energy Agency: Vienna, Austria, 2025. [CrossRef]
61. Humphreys, D. The mining industry and the supply of critical minerals. In *Critical Metals Handbook*, 1st ed.; Gunn, G., Ed.; John Wiley & Sons, Ltd.: Chichester, UK, 2014; pp. 20–40. [CrossRef]
62. Schulz, B. Monazite microstructures and their interpretation in petrochronology. *Front. Earth Sci.* **2021**, *9*, 668566. [CrossRef]
63. Ondrejka, M.; Uher, P.; Putis, M.; Broska, I.; Bacik, P.; Koneèný, P. Two-stage breakdown of monazite by post-magmatic and metamorphic fluids: An example from the Veporic orthogneiss, Western Carpathians, Slovakia. *Lithos* **2012**, *14*, 245–255. [CrossRef]
64. Bamforth, T.G.; Xia, F.; Putnis, A.; Brugger, J.; Hu, S.-Y.; Roberts, M.P.; Suvorova, A.; Pring, A. Hydrothermal mineral replacement in the apatite–rhabdophane–monazite system: Experiments, reaction mechanisms and geological implications. *Chem. Geol.* **2024**, *666*, 122307. [CrossRef]
65. Knorsch, M.; Bamforth, T.G.; Xia, F.; Schoneveld, L.; Roberts, M.P.; Deditius, A.P.; Pearce, M.A. Hydrothermal mineral replacement of bastnäsite by rhabdophane and monazite: Effects of temperature on mineralogy, REE immobilisation, and fractionation. *Contrib. Miner. Pet.* **2024**, *179*, 101. [CrossRef]
66. Williams-Jones, A.E.; Wood, S.A. A preliminary petrogenetic grid for REE fluorocarbonates and associated minerals. *Geochim. Cosmochim. Acta* **1992**, *56*, 725–738. [CrossRef]

67. Cook, N.J.; Ciobanu, C.L.; Wade, B.P.; Gilbert, S.E.; Alford, R. Mineralogy and distribution of REE in oxidised ores of the Mount Weld laterite deposit, Western Australia. *Minerals* **2023**, *13*, 656. [CrossRef]
68. Ciobanu, C.L.; Kontonikas-Charos, A.; Slattery, A.; Cook, N.J.; Ehrig, K.; Wade, B.P. Short-range stacking disorder in mixed-layer compounds: A HAADF STEM study of bastnäsite-parisite intergrowths. *Minerals* **2017**, *7*, 227. [CrossRef]
69. Ciobanu, C.L.; Cook, N.J.; Slattery, A.; Ehrig, K.; Liu, W.Y. Nanoscale intergrowths in the bastnäsite-synchysite series record transition towards thermodynamic equilibrium. *MRS Bull.* **2022**, *47*, 250–257. [CrossRef]
70. Gysi, A.P.; Williams-Jones, A.E. Hydrothermal mobilization of pegmatite-hosted REE and Zr at Strange Lake, Canada: A reaction path model. *Geochim. Cosmochim. Acta* **2013**, *122*, 324–352. [CrossRef]
71. Wang, Z.-Y.; Fan, H.-R.; She, H.-D.; Zhou, L.; Yang, K.-F. Carbonatite-related REE deposits: An overview. *Minerals* **2020**, *10*, 965. [CrossRef]
72. Verplanck, P.L. The role of fluids in the formation of rare earth element deposits. *Procedia Earth Planet. Sci.* **2017**, *17*, 758–761. [CrossRef]
73. Pan, Y.; Fleet, M.E. Compositions of the apatite-group minerals: Substitution mechanisms and controlling factors. *Rev. Miner. Geochem.* **2002**, *48*, 13–49. [CrossRef]
74. Harlov, D.E. Apatite: A fingerprint for metasomatic processes. *Elements* **2015**, *11*, 171–176. [CrossRef]
75. Putnis, A. Mineral replacement reactions: From macroscopic observations to microscopic mechanisms. *Miner. Mag.* **2002**, *66*, 689–708. [CrossRef]
76. Macmillan, E.; Ciobanu, C.L.; Ehrig, K.; Cook, N.J.; Pring, A. Chemical zoning and lattice distortion in uraninite from Olympic Dam, South Australia. *Am. Miner.* **2016**, *101*, 2351–2354. [CrossRef]
77. Macmillan, E.; Ciobanu, C.L.; Ehrig, K.; Cook, N.J.; Pring, A. Replacement of uraninite by bornite via coupled dissolution-reprecipitation: Evidence from texture and microstructure. *Can. Miner.* **2016**, *54*, 1369–1383. [CrossRef]
78. Li, K.; Pring, A.; Etschmann, B.; Xia, F.; Brugger, J. Coupling between mineral replacement reactions and co-precipitation of trace elements: An example from the giant Olympic Dam deposit. *Ore Geol. Rev.* **2020**, *117*, 103267. [CrossRef]
79. King, S.A.; Cook, N.J.; Ciobanu, C.L.; Ehrig, K.; Campo Rodriguez, Y.T.; Basak, A.; Gilbert, S. Coupled microstructural EBSD and LA-ICP-MS trace element mapping of pyrite constrains the deformation history of breccia-hosted IOCG ore systems. *Minerals* **2024**, *14*, 198. [CrossRef]
80. Ansah, E.O.; Jyoti, A.; Black, J.R.; Haese, R.R. The importance of reaction mechanisms and coupled dissolution with reprecipitation (CDR) reactions when modelling copper leaching in heap systems. *Miner. Eng.* **2023**, *203*, 108357. [CrossRef]
81. Altree-Williams, A.; Pring, A.; Ngothai, Y.; Brugger, J. Textural and compositional complexities resulting from coupled dissolution–reprecipitation reactions in geomaterials. *Earth-Sci. Rev.* **2015**, *150*, 628–651. [CrossRef]
82. Burns, P.C.; Finch, R.J. Wyartite: Crystallographic evidence for the first pentavalent-uranium mineral. *Am. Miner.* **1999**, *84*, 1456–1460. [CrossRef]
83. Rodríguez-Villagra, H.; Brendebach, B.; de la Fuente, J.; Alvarez, M.; Missana, T. A snapshot review on uranyl secondary phases formation in aqueous systems. *MRS Adv.* **2023**, *8*, 55–66. [CrossRef]
84. Stanley, D.M.; Wilkin, R.T. Solution equilibria of uranyl minerals: Role of the common groundwater ions calcium and carbonate. *J. Hazard. Mater.* **2019**, *377*, 315–320. [CrossRef] [PubMed]
85. Putnis, A. Mineral replacement reactions. *Rev. Miner. Geochem.* **2009**, *70*, 87–124. [CrossRef]
86. Janeczek, J.; Ewing, R.C. Mechanisms of lead release from uraninite in the natural fission reactors in Gabon. *Geochim. Cosmochim. Acta* **1995**, *59*, 1917–1931. [CrossRef]
87. Guo, X.; Szenknect, S.; Mesbah, A.; Labs, S.; Clavier, N.; Poinssot, C.; Ushakov, S.V.; Curtius, H.; Bosbach, D.; Ewing, R.C.; et al. Thermodynamics of formation of coffinite, $USiO_4$. *Proc. Nat. Acad. Sci. USA* **2015**, *112*, 6551–6555. [CrossRef] [PubMed]
88. Macmillan, E.; Cook, N.J.; Ehrig, K.; Pring, A. Chemical and textural interpretation of late-stage coffinite and brannerite from the Olympic Dam IOCG-Ag-U deposit. *Miner. Mag.* **2017**, *81*, 1323–1366. [CrossRef]
89. Yuan, F.; Jiang, S.-Y.; Liu, J.; Zhang, S.; Xiao, Z.; Liu, G.; Hu, X. Geochronology and geochemistry of uraninite and coffinite: Insights into ore-forming process in the pegmatite-hosted uraniferous province, North Qinling, Central China. *Minerals* **2019**, *9*, 552. [CrossRef]
90. Owen, N.D.; Cook, N.J.; Ram, R.; Brugger, J.; Maas, R.; Schmandt, D.S.; Ciobanu, C.L. Pb-bearing Cu-(Fe)-sulfides: Evidence for continuous hydrothermal activity in the northern Olympic Cu-Au Province, South Australia. *Precambrian Res.* **2023**, *398*, 107225. [CrossRef]
91. Finch, R.J.; Murakami, T. Systematics and paragenesis of uranium minerals. In *Uranium: Mineralogy, Geochemistry and the Environment*; Burns, P.C., Finch, R.J., Eds.; Mineralogical Society of America: Chantilly, VA, USA, 1999; Volume 38, pp. 91–179.
92. Ehrig, K.; Kamenetsky, V.S.; McPhie, J.; Macmillan, E.; Thompson, J.; Kamenetsky, M.; Maas, R. Staged formation of the supergiant Olympic Dam uranium deposit, Australia. *Geology* **2021**, *49*, 1312–1316. [CrossRef]

93. Jackson, L.; Corrick, A.; Zhengdong, H.; Annah, M.; Parbhakar-Fox, A. *Secondary Prospectivity of South Australia's Mine Waste: Review*; Report Book 2023/00031; Department for Energy and Mining: Adelaide, Australia, 2025. Available online: https://catalog.sarig.sa.gov.au/dataset/2023d016570/resource/225924d4-be73-4c0c-878a-c6ca92865737 (accessed on 20 May 2026).
94. Adu, P.C.O.; Dadzie, R.A.; Morrissey, L.; Zanin, M.; Skinner, W.; Abaka-Wood, G.B. Mineralogical constraints and beneficiation perspectives for ultrafine rare earth elements in flotation tailings. *Powder Technol.* **2026**, *479*, 122570. [CrossRef]

**Disclaimer/Publisher's Note:** The statements, opinions and data contained in all publications are solely those of the individual author(s) and contributor(s) and not of MDPI and/or the editor(s). MDPI and/or the editor(s) disclaim responsibility for any injury to people or property resulting from any ideas, methods, instructions or products referred to in the content.